Annual Report April 1, 2015 - March 31, 2016

journal or publication title	University of Tsukuba Tandem Accelerator Complex (UTTAC) Annual Report
number	2015
year	2016
URL	http://hdl.handle.net/2241/00145860

UTTAC-85, 2016

UTTAC

ANNUAL REPORT 2015

TANDEM ACCELERATOR COMPLEX
Research Facility Center for Science and Technology
University of Tsukuba

http://www.tac.tsukuba.ac.jp/

UTTAC

ANNUAL REPORT 2015

April 1, 2015 – March 31, 2016

UTTAC-85, 2016

Editors : Tetsuaki Moriguchi, Kimikazu Sasa,Yoshihiro Yamato, Masumi Matsumura, Masao Sataka, Hiroshi Naramoto, and Hiroshi Kudo

---

UTTAC ANNUAL REPORT is a series of issues, which include annual reports of
Tandem Accelerator Complex, Research Facility Center
for Science and Technology, University of Tsukuba.

Tandem Accelerator Complex, Research Facility Center for Science and Technology,
University of Tsukuba
Tennodai 1-1-1, Tsukuba, Ibaraki 305-8577, Japan

annual@tac.tsukuba.ac.jp

PREFACE

This annual report covers research carried out at the University of Tsukuba Tandem Accelerator Complex (UTTAC) during the fiscal year 2015 (1 April 2015 ~ 31 March 2016), using the 1 MV Tandetron accelerator and radiation source experiments. Additionally, we report on the operation and performance of the new 6 MV tandem-type accelerator, as well as on the test experiments for applied use of the new accelerator.

The main part of the old 12UD Pelletron accelerator was destroyed by the Great East Japan Earthquake on March 11, 2011. Immediately, the government decided to compensate us and we started to plan a new version. The new accelerator was designed by the National Electrostatics Corporation in Middleton, Wisconsin, USA and it arrived in mid-March 2014 at the UTTAC. Before starting to operate the new accelerator, we needed to finish the removal procedure for the damaged accelerator. The procedure was completed with the help of the university office and finally the accelerator operation was started at the beginning of March 2016.

At the end of this fiscal year, The Open Advanced Facilities Initiative supported by the Ministry of Education, Culture, Sports, Science and Technology (MEXT) has been ended. We have very much appreciated this long term government assistance. We would like to continue a similar open facility system by ourselves without financial support. We are looking forward to reporting on our achievements with the new 6 MV accelerator.

Finally, Professor A. Uedono has succeeded the director of UTTAC, effective on 1 April 2016.

Eiji KITA
Director

CONTENTS

5. LIST OF PUBLICATIONS

1.

ACCELERATOR AND RELATED FACILITIES

1.1 Accelerator operation 2015

K. Sasa, S. Ishii, H. Oshima, Y. Tajima, T. Takahashi, Y. Yamato, D. Sekiba, T. Moriguchi, E. Kita

The decommissioning procedure of the 12UD Pelletron tandem accelerator, which was seriously damaged by the Great East Japan Earthquake in 2011 [1], was completed on March 2016 [2]. A new horizontal-type 6 MV Pelletron tandem accelerator was designed and developed by the National Electrostatics Corp., USA in collaboration with the University of Tsukuba. The official inspection of the relevant radiation facility has finished without any problem on March 1, 2016.

In this year, we operated and maintained the 1 MV Tandetron accelerator and the apparatus utilizing radio-isotopes, together with the 6 MV Pelletron tandem accelerator mentioned above. Figure 1 shows a schematic layout of the experimental apparatus at UTTAC. The total service time for facility was 83 days in the fiscal year (FY) 2015.

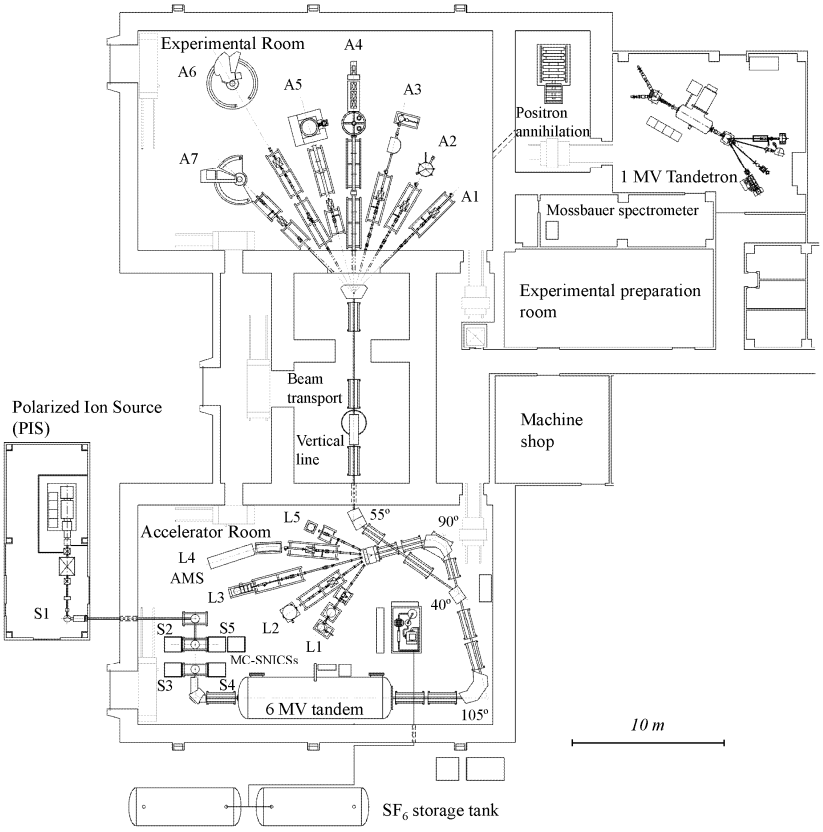

Fig. 1. Schematic layout of the experimental apparatus at UTTAC.

1 MV Tandetron accelerator

The 1 MV Tandetron accelerator has two negative ion sources and four beam lines. It has a permission to apply the terminal voltage up to 1.1 MV. However, the maximum voltage has been limited to below 0.95 MV because of the aged equipment. This also caused the recent instability of the terminal voltage. On November 2015, we replaced RF oscillating pair tubes in the Cockcroft-Walton circuits for the high-voltage generator in order to resolve the voltage instability. The terminal voltage up to 0.95 MV was stabilized after the replacement.

The operating time and the experimental beam time of the 1 MV Tandetron accelerator were 673.7 and 275.8 hours, respectively, during the total service time in FY 2015. Totally 52 research programs were carried out and 552 researchers used the 1 MV Tandetron accelerator. Figure 2 shows the percentage of accelerated ions for the 1 MV Tandetron accelerator. Figure 3 shows the percentage of research fields for the 1 MV Tandetron accelerator.

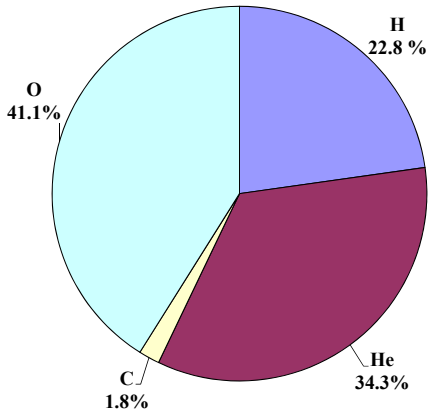

Fig. 2. Percentage of accelerated ions for the 1 MV Tandetron accelerator in FY 2015.

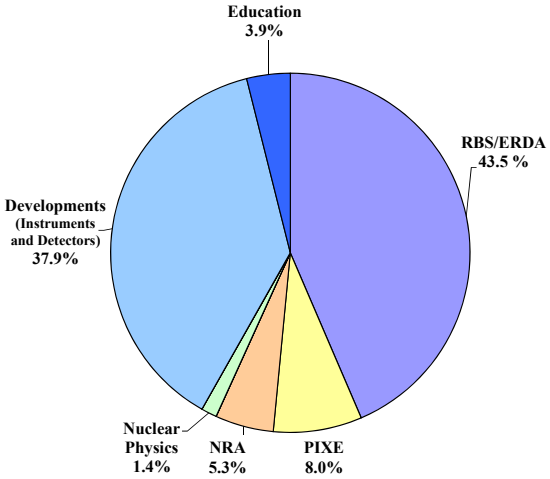

Fig. 3. Percentage of research fields for the 1 MV Tandetron accelerator in FY 2015.

6 MV Pelletron tandem accelerator

Table 1 indicates specifications of the 6 MV Pelletron tandem accelerator installed in the spring of 2014 at UTTAC. We have constructed incidental equipment, infrastructure and beam lines for the 6 MV Pelletron tandem accelerator since 2014. The facility of the 6 MV Pelletron tandem accelerator is shown in Fig. 4. The 6 MV Pelletron tandem accelerator is used for AMS, IBA, microbeam applications, high-energy ion irradiation and nuclear physics [3].

Table 1. Specifications of the 6 MV Pelletron tandem accelerator.

- Model: 6 MV Pelletron Tandem
  (18SDH−2, National Electrostaics Corp., USA)
- Accelerator Tank Size: Length: 10.5 m
  Diameter: 2.74 m
  Line Height: 1.78 m
  Weight: 20,865 kg
- Terminal Voltage: 1.0 − 6.5 MV
- Voltage Ripple: ≤ 750 V p−p at 6.0 MV
- Voltage Control: GVM & Slit Current Feedback System
- Maximum Beam Current: H : 3 μA
  Heavy ions: ~50 μA
- Terminal Stripper: Gas (Ar or N_2)
  Foil Unit (80 Foil Holders)
- Insulation Gas: SF_6 (0.6 MPa)
- Beam Courses : 12 Lines and Vertical Transport Line
- Ion Sources:
  Cs Sputtering Negative Ion Sources
  NEC SNICS II
  NEC MC-SNICS
  NEC CO_2 Gas Type MC-SNICS
  RF Ion Source (NEC Alphatross)
  Lamb-shift Polarized Negative Ion Source
- Mass Energy Product (ME/Z^2): 15 amu MeV (LEBT)
  176 amu MeV (HEBT)

Fig. 4. Photograph of the facility of the 6 MV Pelletron tandem accelerator.

We got an authorization of management change for the radiation facility from the Nuclear Regulation Authority on Sept. 2015. After the adjustment of training and operation, we got a permission to use the 6 MV Pelletron tandem accelerator from the Nuclear Safety Technology Center on January 2016. Routine beam delivery for experiments has started on March 1, 2016. The electric generator operates up to the terminal voltages of 6.5 MV. Its stability is estimated to be better than 1 kV at a 6.0 MV terminal voltage. Maximum beam currents are expected to be up to 3.0 μA for protons and 50 μA for heavy ions.

The operating time and the experimental beam time of the 6 MV Pelletron tandem accelerator were 725.9 and 62.4 hours, respectively, during the total service time in FY2015. Figure 5 shows the beam time histogram with respect to the terminal voltage. Totally 9 research programs were carried out and 60 researchers used the 6 MV Pelletron tandem accelerator on March 2016. Total experimental time was 17 days in FY 2015. Figure 6 shows the percentage of accelerated ions. The percentage of research fields for the 6 MV Pelletron tandem accelerator is shown in Fig. 7.

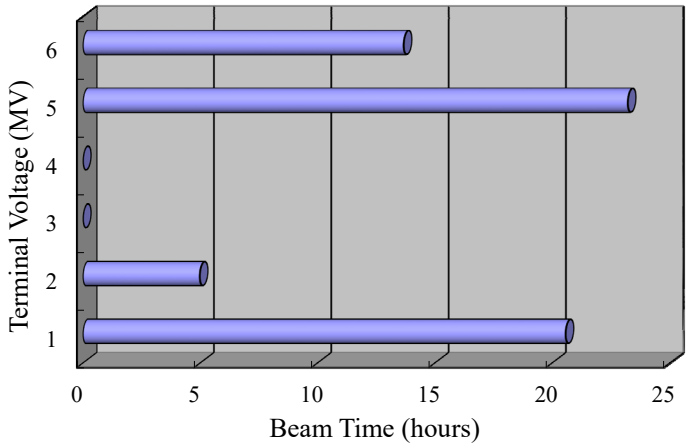

Fig. 5. Beam time histogram as a function of the terminal voltage for the 6 MV Pelletron tandem accelerator in FY 2015.

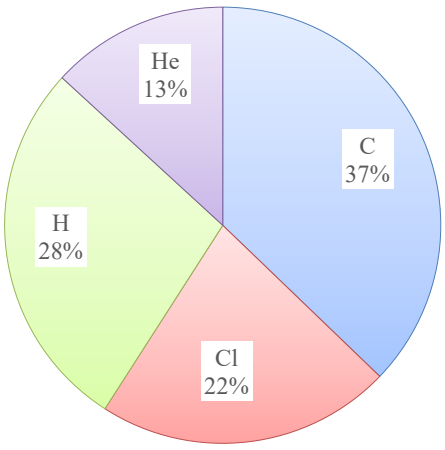

Fig.6. Percentage of accelerated ions for the 6 MV Pelletron tandem accelerator in FY 2015.

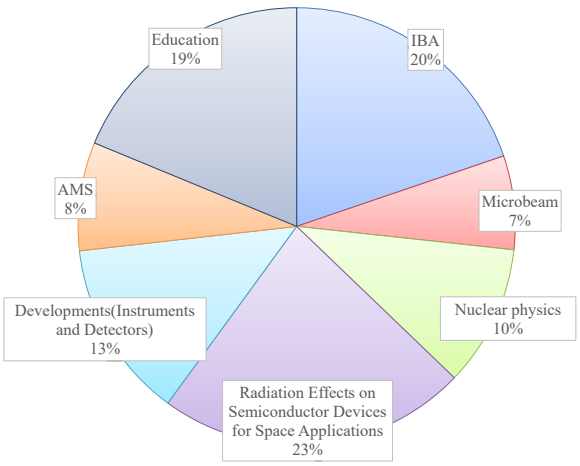

Fig. 7. Percentage of research fields for the 6 MV Pelletron tandem accelerator in FY 2015.

References

[1] K. Sasa, AIP Conf. Proc.1533 (2013) 184-188.

[2] T. Moriguchi et al., this annual report.

[3] K. Sasa et al., JACoW, Proceedings of HIAT2015 (2015) 285-287.

1.2 Decommissioning of the 12UD Pelletron Tandem Accelerator

T. Moriguchi, K. Sasa, H. Oshima, S. Ishi, T. Takahashi, Y. Tajima, Y. Yamato, D. Sekiba, E. Kita, A. Uedono

Since 1975, the 12UD Pelletron tandem accelerator has been in operation for researches and student's education at University of Tsukuba. This machine, however, was damaged seriously by the Great East Japan Earthquake on 11 March 2011 [1], so that we decided to shut down this accelerator. This is partly because it has already been replaced by a new accelerator. For shutdown of the accelerator, it is necessary to treat radioactivated materials legally under the law (Act on Prevention of Radiation Hazards due to Radioisotopes). This is due to the law revision enforced on 1st April 2012. In this revision, "radioactivated materials" were added to the law as control subjects. We proceeded to the decommission procedure of the 12UD Pelletron tandem accelerator under the revised law.

Firstly, we performed calculations by using the Monte Carlo simulation code PHITS and DCHAIN-SP in order to investigate the range of induced radioactivity [2]. In this calculation, we assumed the accelerator's condition for maximum activation. Protons and deuterons were employed as projectile ions in the calculation. The irradiation time in the calculation was referenced from the operation log books of the accelerator. The terminal voltage was set to 10.5 MV, which is the actual maximum voltage. Duration of the accelerator operation was set to 39 years from 1976 to 2014, as well as no operation for the four years from 2011 to 2014. Figure 1 shows the produced nuclei and these radioactivity obtained by the calculation both in the SUS frame, which supports electron stripper foils made of carbon, and the beam duct in the accelerator tank. Bold bars in Fig. 1 indicate the clearance levels of the nuclides determined by the law. The values in the brackets in Fig. 1 indicate the sum of the ratio between the radioactivity obtained by the calculation and the clearance level. If this value of one object is higher than unity, we regarded it as a radioactivated material in the present calculation. With this criterion, the SUS frame was regarded as a radioactivated material, but the beam duct was not, as shown in Fig. 1.

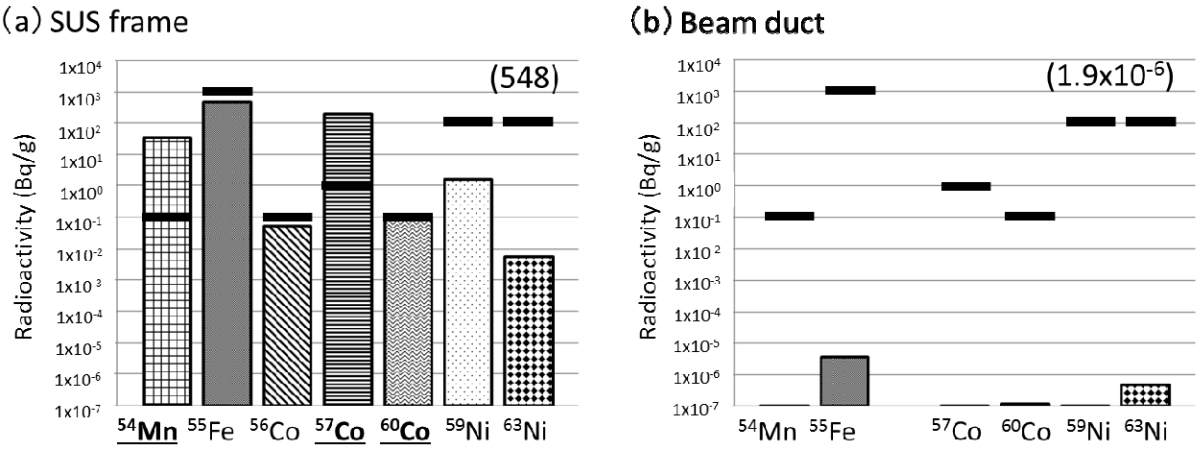

Fig. 1. Radioactivity obtained by the calculation (see the text for details).

Secondly, we confirmed the results of calculation by measurements with a NaI surveymeter (TCS-172B). The time constant of the survey meter, measurement time and distance between the survey meter and an object were set to ten seconds, thirty seconds and five mm, respectively [3]. In order to judge whether an object is activated or not, we employed the counting rate of the detection limit as follows.

$$N_{\mathrm{d}} = \frac{K}{2}\left\{\frac{K}{t_{\mathrm{s}}} + \sqrt{\left(\frac{K}{t_{\mathrm{s}}}\right)^2 + 4N_{\mathrm{b}}\left(\frac{1}{t_{\mathrm{s}}} + \frac{1}{t_{\mathrm{b}}}\right)}\right\}$$

N_{d} : Counting rate of the detection limit
K : Coefficient of standard deviation ($K = 3$)
N_{b} : Counting rate of the background
t_{s} : Measurement time of the sample
t_{b} : Measurement time of the background

If the counting rate of one object after subtracting that of the background is higher than N_{d}, we regarded it as a radioactivated material. Objects regarded as radioactivated materials by the calculation were measured by a germanium detector for nuclide identification.

Table 1 shows summary of the calculation and the measurement for nineteen objects in the accelerator room, the analyzing magnet room and the measurement room. In the cases of slits, Faraday cups and beam stopper, we disassembled one object into two parts; one is a part irradiated directly by beams, the other is a remaining part. For example, “Object slit” and “Object slit (duct)” in Table 1 indicate four elements which are irradiated directly by beams and the remaining part, respectively, as shown in Fig. 2. As shown in Table 1, the results of calculation are confirmed by measurements except for the SUS frames. In the case of the SUS frames, they are thought to be less irradiated, and accordingly, less activated than expected from the calculation. Radioactivated materials including the SUS frames were packed properly and delivered to Japan Radioisotope Association. Since the flanges of switching magnet were reused as an object of the beam line of a new accelerator, nuclide identification using a germanium detector was not performed. From calculations and measurements, we found that objects irradiated indirectly by beams were activated, but the other parts were not activated in the case of the 12UD Pelletron tandem accelerator.

Finally, after removing the radioactivated materials, we confirmed with survey meters that floors, walls and beamlines in the accelerator building were not activated. The 3rd to 7th floors of the accelerator building were excluded from the radiation controlled area.

So far, there are few cases of decommissioning of accelerators on the revised law, like in the present case. This is a useful example to be referred in future.

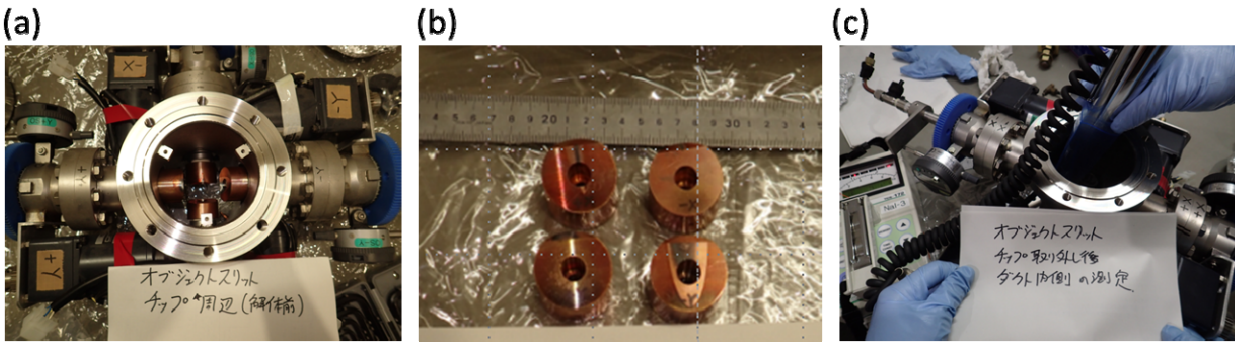

Fig. 2. Pictures of the object slit. (a)Before disassembling. (b)Four elements. (c)Measurement of radioactivity for the assembly after removing four elements.

Table 1. Summarized results of radioactivity evaluation based on calculation and measurements.

			Calculation		Measurement	
Room	Object	Material	Result	Nuclide	Result	Nuclide
Accelerator room	#01 SUS frame	Stainless steel	Activated	^{57}Co, ^{54}Mn, ^{60}Co	No activated	^{57}Co, ^{54}Mn, ^{60}Co
	#02 Beam duct (up)	Stainless steel	No activated	–	No activated	–
	#03 Beam duct (down)	Stainless steel	No activated	–	No activated	–
	#04 Terminal shell	Stainless steel	No activated	–	No activated	–
	#05 Tank (center)	Steel	No activated	–	No activated	–
	#06 Tank (bottom)	Steel	No activated	–	No activated	–
Analyzing magnet room	#07 Object slit	Copper	Activated	^{60}Co, ^{65}Zn	Activated	^{60}Co, ^{65}Zn, ^{22}Na
	#08 Object slit (duct)	Stainless steel	No activated	–	No activated	–
	#09 Image slit	Tantalum	Activated	^{179}Ta, ^{181}W	Activated	^{210}Pb, ^{22}Na
	#10 Image slit (duct)	Stainless steel	No activated	–	No activated	–
	#11 Faraday cup	Tantalum	Activated	^{179}Ta, ^{181}W	Activated	^{181}W, ^{210}Pb, ^{22}Na
	#12 Faraday cup (duct)	Stainless steel	No activated	–	No activated	–
	#13 Flange of switching magnet	Stainless steel	Activated	^{57}Co, ^{54}Mn, ^{60}Co, ^{55}Fe	Activated	–
Measurement room	#14 Course slit 1	Copper	Activated	^{60}Co, ^{65}Zn	Activated	^{60}Co, ^{65}Zn, ^{22}Na
	#15 Course slit 1 (duct)	Stainless steel	No activated	–	No activated	–
	#16 Course slit 2	Copper	Activated	^{60}Co, ^{65}Zn	Activated	^{60}Co, ^{65}Zn
	#17 Course slit 2 (duct)	Stainless steel	No activated	–	No activated	–
	#18 Beam stopper	Tantalum	Activated	^{181}W	Activated	^{182}Ta, ^{181}W, ^{210}Pb
	#19 Beam stopper (duct)	Stainless steel	No activated	–	No activated	–

References

[1] K. Sasa et al., UTTAC Annual Report 2010 (2011) 1.

[2] T. Sato et al., J. Nucl. Sci. Technol. 50:9 (2013) 913.

[3] Y. Uwamino, Japanese Journal of Radiation Safety Management 12:1 (2013) 36.

1.3 First beam transport through the ion microbeam line from the 6 MV tandem accelerator

A. Yamazaki, K. Sasa, S. Ishii, M. Kurosawa, S. Tomita, A. Uedono, E. Kita

Some characteristics of inorganic materials are strongly affected by light elements contained. Therefore, observation of these elements is important for research and development of new materials. With this as a background, setup of apparatus to observe or even visualize light elements in a material is widely required.

Ion beam analysis techniques are powerful tools for characterizing elemental concentration quantitatively. Particle induced X-ray emission (PIXE) is one of useful methods for elemental analysis and is in particular suitable for detecting trace elements. This is due to the high signal-to-background ratio, compared with the case of electron-induced emission. Combining PIXE with a microbeam scanning technology, we can obtain two-dimensional maps of trace elements in a sample material. Setup of microbeam PIXE apparatus should provide a useful as well as powerful tool for materials research and development.

In UTTAC, a new 6 MV tandem accelerator has been installed in the early 2015, and succeedingly several beam lines have been constructed. One of them is the ion microbeam irradiation line and its construction has been completed in February 2016. This has been connected to the 0 degree beam course after the switching magnet of the 6 MV tandem accelerator beam line. A submicron microbeam scanning end stage OM-2000 (Oxford Microbeams Ltd., UK) has been installed at the end of this line. This end stage consists of beam defining slits, ferrite cored pre-lens deflector coils for X-Y scan, a triplet of magnetic quadrupole lenses and a target irradiation chamber with a three-axis target positioning device.

Test experiments for transporting and focusing ion beam have started in March 2016. A 3 MeV proton beam was transported from the 6MV tandem accelerator to the microbeam line and collimated by a double collimator slits. The distance between the two slits is 7820 mm and that from the first slit to the target position is 8730 mm. The collimated proton beam was focused by the quadrupole magnetic lenses and was irradiated onto a CaF_2 crystal with the thickness of 0.5 mm positioned at the center of the irradiation chamber. The working distance (distance from the end of the quadrupole lenses to the target) is 180 mm. A photograph of the ion microbeam line is shown in Fig. 1.

A fluorescence caused by the irradiation of the CaF_2 crystal was observed by a CCD camera with a high-power lens from the opposite side of the beam irradiation surface. After optimization of beam transporting parameters and precise alignment of the quadrupole triplet lenses, we obtained a square beam spot with about 100 μm wide and an ellipsoidal spot with about 30 μm wide. We are going to obtain an ion beam of 1 μm in diameter on target by the end of FY2016.

Acknowledgement

The authors would like to thank technical experts H. Iso and Y. Higuchi of Neos Tech Co., Ltd. for their valuable advice and various technical supports. This work is supported by Cross-Ministerial Strategic Innovation Promotion Program - Unit D66 - Innovative measurement and analysis for structural materials (SIP-IMASM) operated by the cabinet office.

Fig. 1. Photograph of the ion microbeam line at UTTAC.

2.

NUCLEAR AND ATOMIC PHYSICS

2.1 Measurements of magnetic moments for unstable nuclei in AVF, RCNP

Y. Ishibashi, D. Nagae[1], Y. Abe[1], Y. Ichikawa, T. Moriguchi, S. Suzuki, Y. Tajiri, A. Ozawa, H. Ueno[1]

The nuclear moment is one of the most important observables of the nuclear structure. For the measurements of the nuclear magnetic dipole moment (μ) of unstable nuclei, β-ray-detected nuclear magnetic resonance (β-NMR) method [1] is effectively used. In this work, we report a target study on the measurement of μ moment of ^{40}Sc by means of the β-NMR method at the Research Center for Nuclear Physics, Osaka University. In the β-NMR method, unstable nuclei must be spin-polarized. A spin-polarized ^{40}Sc nucleus was produced in the ^{40}Ca($\vec{p}$,n)^{40}Sc reaction. In the reaction, the polarization of the beam particles is transferred to each nucleus. A $\vec{p}$ beam was produced using a polarized ion source [2], and accelerated at $E = 72$ MeV using AVF cyclotron. The polarized protons were irradiated on a CaS, a CaO, and a CaF_2 targets to produce the polarized ^{40}Sc. The targets were placed at the center of the β-NMR apparatus at room temperature.

The higher the purity of ^{40}Sc, the more efficiently it can be measured; therefore, we performed purity measurement and comparison of the three targets. The β-rays emitted from ^{40}Sc were detected with plastic scintillator telescopes located above and below the targets. In order to deduce the purity of the ^{40}Sc, half-lives were measured using three targets. Figure 1(a), 1(b), and 1(c) are β-decay time spectra obtained using CaS, CaO, and CaF_2 targets, respectively. The time spectra obtained from the accumulated β rays in the ^{40}Sc experiment were fitted with two or three exponential functions in addition to a constant background arising from the long-lived impurities. The least squares method was applied to the analysis. The results of the fitting analysis are shown in Fig. 1(a), 1(b), and 1(c). The observed half-lives were slightly longer than the reported half-life of 182.3(7) ms. The estimated contaminations of ^{32}Cl($T_{1/2}$ = 298 ms), ^{29}P($T_{1/2}$ = 4.142 s), ^{13}N($T_{1/2}$ = 9.965 m), and ^{37}K($T_{1/2}$ = 1.225 s) have much longer half-lives than that of ^{40}Sc. Thus, the ^{40}Sc isotopes were correctly produced in the ^{40}Ca($\vec{p}$,n)^{40}Sc reaction. The purities of the ^{40}Sc are obtained to be 23^{+36}_{-23}%, 23^{+33}_{-23}%, and 37$\pm$4% using CaS, CaO, and CaF_2 targets, respectively.

From the half-life measurements, the purity of the ^{40}Sc using CaF_2 was determined to be the highest. Thus, we applied a CaF_2 target for the measurement of the μ moment of ^{40}Sc by the β-NMR method. In order to maintain the spin polarization, a static magnetic field B = 543 mT was applied. The up/down ratio R of the β-ray counts is written as $R_0 \sim a(1+A_\beta P)/(1-A_\beta P)$, where a, A_β, and P denote a constant factor representing asymmetries in counter solid angle and efficiencies, the β-ray asymmetry parameter, and the degree of spin-polarization, respectively. An oscillating magnetic field perpendicular to the static field was applied to the CaF_2 target using an rf coil. If the frequency of the rf field corresponds to the resonance field for the spin-polarized ^{40}Sc, the direction of the spin polarization is changed by the NMR. Then, the ratio changes to $R \sim a(1-A_\beta P)/(1+A_\beta P)$. The β-ray asymmetry $A_\beta P$ is written as $A_\beta P = \sqrt{(R_0/R)-1}/\sqrt{(R_0/R)+1}$. The μ moment is derived from the frequency of the observed peak or dip in the $A_\beta P$ spectrum. The analysis is in progress.

[1]RIKEN Nishina Center

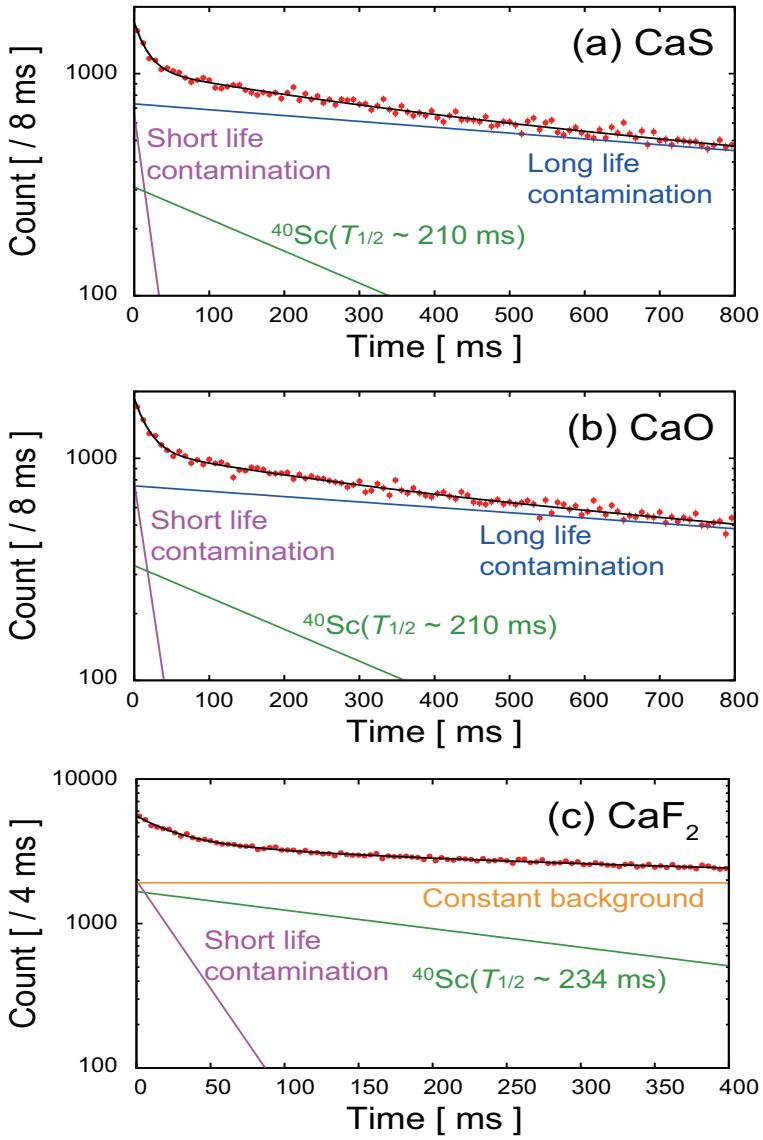

Fig. 1. β decay spectra for ^{40}Sc in different three targets (CaS, CaO and CaF_2.)

References

[1] K. Sugimoto et al., J. Phys. Soc. Jpn. **21** (1966) 213.

[2] K. Hatanaka et al., Nucl. Instr. and Meth. **217** (1983) 397.

2.2 Production of unstable nuclei ^{25}Al and ^{30}P via resonant proton-capture reactions

T. Matsumoto, K. Hiraishi, A. Ozawa, Y. Ichikawa, T. Moriguchi, S. Suzuki, Y. Tajiri

The proton-capture reactions have been investigated for long time for various stable nuclei and in the various energy range. In the point of production of unstable nuclei, the resonant proton-capture reactions are attractive. In the UTTAC, Lamb-shift type polarized ion source, where polarized proton beams are available, is installed. If the polarized protons are captured, reaction products will be highly polarized. If the products are unstable nuclei, we may obtain highly polarized unstable nuclei and can determine nuclear moments for these nuclei by using β-NMR method.

Thus, by the above motivation, we started investigation of resonant proton-capture reactions at UTTAC [1]. In this fiscal year, we investigated following two reactions by using natural Mg and Si targets, respectively; ^{24}Mg(p,γ)^{25}Al(I=5/2$^+$, $T_{1/2}$=7.1 s) and ^{29}Si(p,γ)^{30}P(I=1$^+$, $T_{1/2}$=150 s). The resonant proton-capture reactions for ^{25}Al and ^{30}P have been well investigated [2, 3]. Purposes of the present experiment were to check effective yields and contaminants. We used proton beams of E_p=860 keV accelerated in 1 MV tandem accelerator. We used natural Mg target for ^{25}Al production, and natural Si target for ^{30}P production. Thicknesses of the targets were 0.32 mm (Mg) and 0.51 mm (Si), respectively. A typical proton-beam current was 1 μA. γ-rays from reaction products were measured by two HP-Ge detectors. We calibrated energy and detection efficiencies for the Ge detectors by using ^{152}Eu source. We irradiated the protons for about 1500 and 1800 s to Mg and Si targets, respectively.

Since the target is thick enough to stop the proton beams, for ^{24}Mg in the Mg target, three resonances (E_r: resonance energy) E_r=223, 419 and 823 keV can be observed [2]. On the other hand, for ^{29}Si in the Si target, four resonances E_r=333, 414, 695 and 730 keV can be observed [3]. In each resonance, from the produced corresponding excited-states specific γ-rays are injected. For example, for ^{24}Mg in the Mg target, E_γ=2610 keV can be observed for the resonance with E_r=823 keV, as shown in Fig. 1. We integrated events in the peak, taking into account detection efficiencies for the Ge detectors. Thus, we evaluated the yield for ^{25}Al in this resonance. As mentioned before, since three resonances can occur for ^{24}Mg in the Mg target, we summed the yields for the three resonances. The same procedure was done for ^{30}P.

Estimated total production yields for ^{25}Al and ^{30}P are about 1800 cps/μA and 160 cps/μA, respectively. For the ^{30}P case, natural abundance of ^{29}Si is only 4.7 %, thus contaminants from ^{28}Si (92.0%) and ^{30}Si (3.0%) should be considered. In E_p = 860 keV, one resonance (E_r=327 keV) can occur for ^{28}Si and five resonances (E_r=500, 625, 675 775 and 840 keV) can occur for ^{30}Si. We also observed γ-rays related to these resonances. We estimated total production yields for ^{29}P and ^{31}P from the observed γ-rays. The total production yields for ^{29}P and ^{31}P are about 30 and 380 cps/μA, respectively. It is noted that ^{31}P is a stable nucleus but ^{29}P has β-radioactivity (I=1/2$^+$) with $T_{1/2}$=4.1 s. For the ^{25}Al case, natural abundance of ^{24}Mg is 79.0 %. We considered contaminants from ^{25}Mg (10.0%) and ^{26}Mg (11.0%). At E_p= 860 keV, many resonances can occur since there are many excited states in ^{26}Al and ^{27}Al, respectively. It is noted that in ^{26}Al there is an isomer (^{26m}Al, E_x=228 keV, I=0$^+$) with $T_{1/2}$=6.3 s. We observed several γ-rays related to the

excited states in both nuclei (E_γ=1843, 1622 and 829 keV for ^{26m}Al, E_γ=417 keV for ^{26}Al and E_γ=8036, 6821, 3957, 2982, 1015 and 844 keV for ^{27}Al). Thus, we can estimate production yields (lower limit) for these nuclei. Presently observed production yields are 350 cps/μA (^{26m}Al), 540 cps/μA (^{26}Al) and 2100 cps/μA (^{27}Al), respectively.

From the observed production yields and contaminants for ^{25}Al and ^{30}P, we noticed that determination of nuclear moments by β-NMR method for these nuclei are quite feasible. Since the electric quadrupole moment of ^{25}Al and the magnetic dipole moment of ^{30}P are unknown, we will measure the moments by using the resonant proton capture reactions with polarized proton beams at UTTAC.

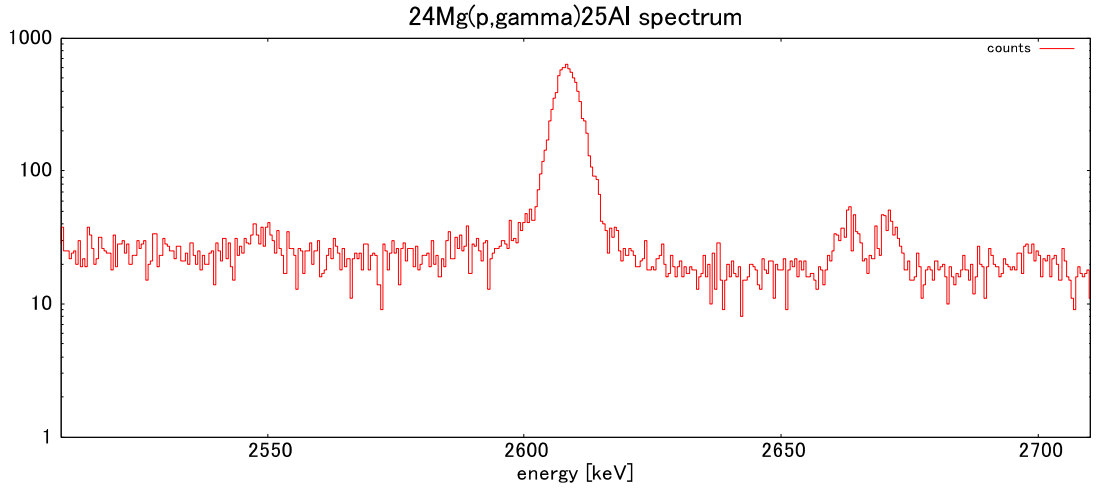

Fig. 1. γ-ray spectrum of E_γ=2610 keV observed in the present experiment with the Mg target in E_p=860 keV. This γ-ray corresponds to that injected from the excited state with E_x=3062 keV in ^{25}Al produced by the resonant ^{24}Mg(p,γ)^{25}Al reaction.

References

[1] A.Ozawa et al., UTTAC Annual Report 2014 (2015) 12.

[2] D.C. Powell et al., Nucl. Phys. A 660 (1999) 349 and references therein.

[3] J.P.L. Reinecke et al., Nucl. Phys. A 435 (1985) 333 and references therein.

2.3 Target thickness dependence of convoy electron yield observed in fast cluster ion bombardment on thin foils

Y. Shiina, R. Kinoshita, M. Matsuda[1], M. Imai[2], K. Kawatsura[3], M. Sataka, K. Sasa, S. Tomita

Electronic excitation due to penetration of swift cluster ions through solids are different from that of atomic ions in some ways. For example, it is reported that convoy electron yields per constituent atom increase proportionally to the size of impinging clusters under 0.5 MeV/atom C_n^+ ion bombardment (n=1-4) on thin C foils [1]. On the other hand, low-energy secondary electron yields in cluster ion bombardments are suppressed by about 20-50% compared with those in bombardments of equal-velocity atomic ions. These previous studies suggest that the electron transport mechanism inside the material is affected by multiple projectile ions which are closely spaced with each other. In this work, thin C foils were bombarded with 3.5 MeV/atom C_n^+ cluster ions to investigate target thickness dependence of convoy electron yields.

Our experiments were performed at the 20-MV tandem accelerator in the Nuclear Science Research Institute of Japan Atomic Energy Agency (JAEA). A schematic diagram of the experimental setup is shown in fig. 1. The C_n^+ ions (n=1-3) were accelerated to an energy of 3.5 MeV/atom and impinged on amorphous carbon foils. Thicknesses of carbon foils were 3.1, 4.8, 10.5, 19.5 and 29.7 μg/cm^2. The energies of electrons emitted to the beam direction were analyzed by a tandem-type 45° parallel-plate electrostatic spectrometer with the pass energy fixed to 50 eV. The relative energy resolution of the spectrometer is 3.2%, which corresponds to 1.6 eV in absolute energy. The beam current was monitored by a Faraday cup placed behind the spectrometer to normalize electron energy spectra.

Target thickness dependence of convoy electron yields is shown in fig. 2. For all targets, convoy electron yields increased with larger cluster size, agreeing qualitatively with our previous results on 0.5 MeV/atom C_n^+ bombardments [1]. In atomic ion bombardments, convoy electron yields slightly increased with thicker target foil, probably owing to normalization using the Faraday cup. In C_2^+ and C_3^+ bombardments, convoy electron yield decreases as target thickness increases from 3.1 to 10.5 μg/cm^2. C_3^+ ion bombardments are more significant, where the convoy electron yield decreases by about 40% as target thickness increases from 4.8 to 10.5 μg/cm^2. Moreover, the attenuation length of convoy electrons is evidently longer for C_3^+ ions than for C_2^+ ions. Attenuation length of convoy electrons is reported longer than that of free electrons due to frequent transition between continuum and discrete states [2]. The present result may suggest that low-energy electrons in the projectile rest frame are delocalized and affected by multiple projectile ions simultaneously.

[1] Japan Atomic Energy Agency (JAEA)
[2] Kyoto University
[3] Theoretical Radiation Research Laboratory

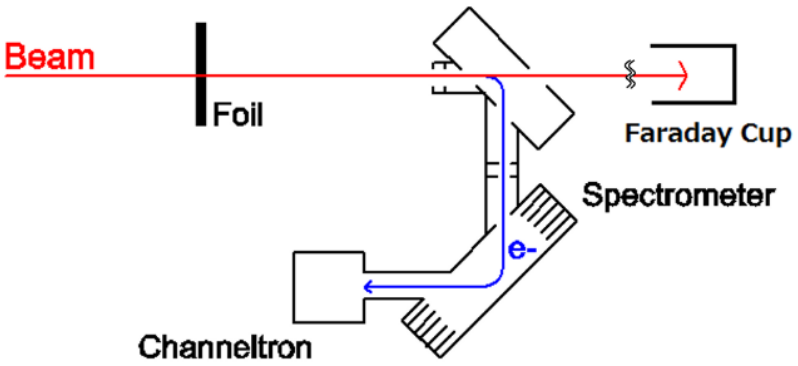

Fig.1. A schematic diagram of the experimental setup.

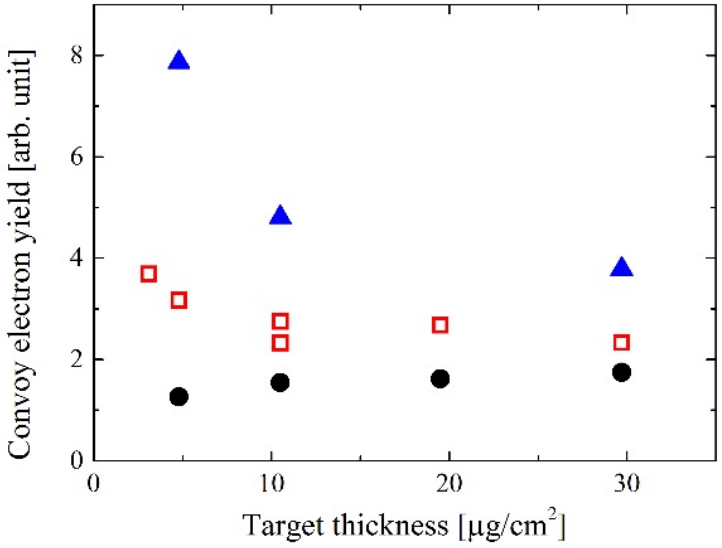

Fig.2. Target thickness dependence of convoy electron yield in 3.5 MeV/atom C^+ (circles), C_2^+ (squares), C_3^+ (triangles) bombardments on thin C foils.

References

[1] S. Tomita, S. Yoda, R. Uchiyama, S. Ishii, K. Sasa, T. Kaneko and H. Kudo, Phys. Rev. A 73 (2006) 060901.

[2] J. Burgdorfer, Lecture Notes in Physics 294 (1988) 344.

3.

ACCELERATOR MASS SPECTROMETRY

3.1 Detection tests of rare particles by the 6 MV tandem accelerator mass spectrometry system

K. Sasa, T. Takahashi, T. Matsunaka, M. Matsumura, S. Hosoya, K. Sueki, M. Stodola[1], M. Sundquist[1]

The rare-particle detection system on the 6 MV Pelletron tandem accelerator (Tsukuba 6 MV AMS system) was designed and constructed for the high-sensitivity detection of ^{10}Be, ^{14}C, ^{26}Al, ^{36}Cl, ^{41}Ca, and ^{129}I, and is also expected to measure other radioisotopes ^{32}Si and ^{90}Sr [1]. It has two Cs sputtering negative ion sources: a 40-sample MC-SNICS for the routine measurement of all nuclides and a hybrid source with a 39-sample MC-SNICS equipped with a CO_2 gas introduction system with either graphite or CO_2 samples for ^{14}C AMS. The main accelerator (model 18SDH-2 Pelletron accelerator developed by NEC, USA) has a long gas stripper tube assembly and a foil changer with 80 foil holders for equilibrium stripping ions. Carbon stripper foils will be mainly used for ^{36}Cl and ^{41}Ca AMS to obtain highly-charged positive ions. The rare-particle detection system has a 22.5° ESA (3.81 m radius) with a resolution of E/ΔE = 200. A five-electrode gas ionization detector [2, 3] is installed on the end station of the rare-particle detection system. Figure 1 shows a schematic view of the Tsukuba 6 MV AMS system.

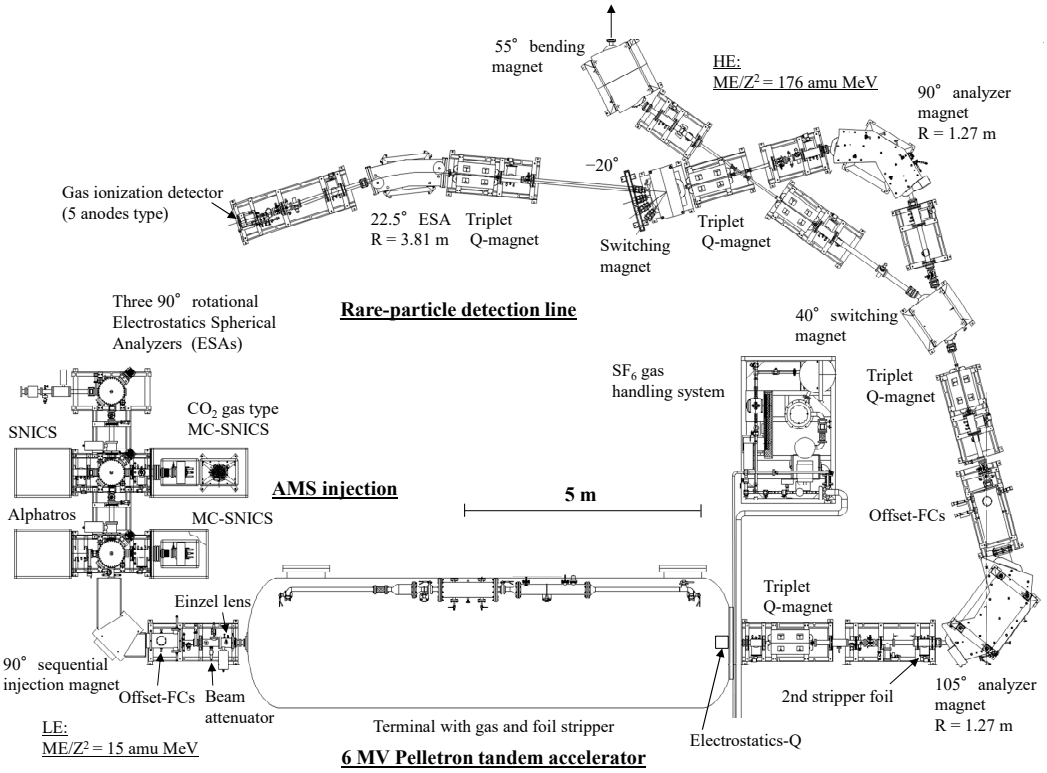

Fig.1. Schematic view of the Tsukuba 6 MV AMS system.

The first experiment of multi-nuclide AMS such as ^{14}C and ^{36}Cl was performed on March 2016. The background of the system for ^{14}C measurements using the 4+ charge state at 5.0 MV was reached to $^{14}C/^{12}C = 4.0 \times 10^{-16}$ (0.04 pMC). ^{36}Cl measurement was performed with carbon foil stripping into the 7+

[1] National Electrostatics Corp., USA

charge state at 6.0 MV. 48.0-MeV $^{36}Cl^{7+}$ was injected into the gas ionization detector. We used a 75-nm-thick Si_3N_4 foil for the entrance window of the gas ionization detector, and the optimal isobutane gas pressure is estimated to be 28 Torr for $^{36}Cl/Cl$. The ^{36}Cl was clearly separated from the ^{36}S in the gas ionization detector. Figure 2 shows a 2-dimentional spectrum for ^{36}Cl AMS with a standard sample of $^{36}Cl/Cl = 1.00 \times 10^{-11}$ [4]. The background of ^{36}Cl reached as low as $^{36}Cl/Cl = \sim 10^{-15}$. Results of the first test are summarized in Table 1, which demonstrates isobar separation performances of the Tsukuba 6 MV AMS system for ^{14}C and ^{36}Cl AMS.

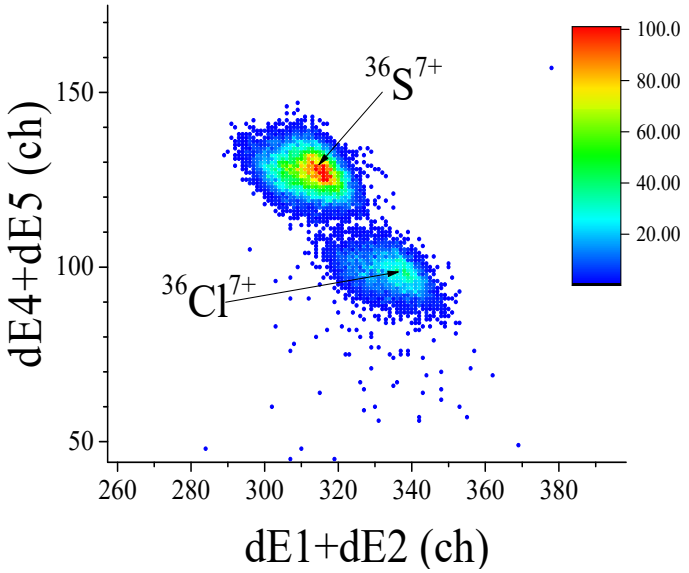

Fig.2. ^{36}Cl AMS spectrum with a standard sample of $^{36}Cl/Cl = 1.00 \times 10^{-11}$. A total of 6,600 counts for ^{36}Cl is detected during the measurement time of 3 min.

Table 1. Performances of the Tsukuba 6 MV AMS system in the trial measurements of ^{14}C and ^{36}Cl.

Isotopes	**^{14}C**	**^{36}Cl**
Target	Graphite	AgCl
Injected ion	C^-	Cl^-
Injectable ion current (μA)	50	30
Detected ion/stripper	$^{14}C^{4+}$ (Gas)	$^{36}Cl^{7+}$ (Foil)
Terminal voltage (MV)	5.0	6.0
Beam Energy (MeV)	25.0	48.0
Transmission (%)	60	5
Background	4.0×10^{-16}	$\sim 2 \times 10^{-15}$
Precision (%)	0.2	3

References

[1] K. Sasa et al., Nucl. Instr. Meth. Phys. Res. B 361 (2015) 124-128.

[2] C. Maden et al., Nucl. Instr. Meth. Phys. Res. B 59 (2007) 131-139.

[3] S. Hosoya et al., this annual report.

[4] P. Sharma et al., Nucl. Instr. Meth. Phys. Res. B 52 (1990) 410-415.

3.2 ^{41}Ca-AMS measurement in UTTAC AMS system

Seiji Hosoya, Kimikazu Sasa, Tetsuya Matsunaka, Masumi Matsumura, Tsutomu Takahashi,
Mark Sundquist [1], Mark Stodola [1], Keisuke Sueki

Accelerator mass spectrometry (AMS) is an ultra-sensitive technique to measure rare isotopes. We have previously measured ^{14}C, ^{26}Al, and ^{36}Cl using the 12UD Pelletron tandem accelerator at UTTAC [1]. After renewing the tandem accelerator [2], we are trying to develop multi-nuclide AMS measurement, for example ^{10}Be, ^{14}C, ^{26}Al, ^{36}Cl, ^{41}Ca and ^{129}I. ^{41}Ca is a long-lived radionuclide ($T_{1/2} = 1.04 \times 10^5$ yr), and can be mainly formed by neutron capture reaction of ^{40}Ca(n, γ)^{41}Ca with secondary cosmic ray. ^{41}Ca is one of Long-Lived Radio Nuclides (LLRN) to clarify the concentration in nuclear waste for their long-term management. The radiological characterization of nuclear waste is essential for managing storage sites. ^{41}Ca is also useful as a biological tracer for bone resorption [3] and as cosmogenic nuclide tracers for the environmental research. However, ^{41}Ca AMS is difficult because of interference by its isobar ^{41}K. It is necessary to suppress isobaric interference by various methods. One such method is the optimization of the detector to separate the ^{41}K contribution from that of ^{41}Ca. Usually, the gas counter detector has only one anode plate to identify the atomic number (Z), because the energy loss of heavy ions depends on Z. However, it is difficult to separate species with similar Z. A multi-plate gas counter can measure the energy loss at each plate, enabling a two-dimensional plot to be constructed by combining two regions of energy loss. This allows identification of species with similar Z. Changing the gas pressure in the detector can alter the separation between the ^{41}K and ^{41}Ca spectra. Therefore, we investigated the appropriate gas pressure using the PHITS [4].

A five-anode-type gas-ionization detector (Fig. 1) is used for the new 6 MV AMS system of UTTAC. The PHITS simulation gave an optimum isobutane pressure range of 18-25 Torr. Figure 2 shows measurement results in isobutane at different pressure, 24 and 11 Torr. Regarding the peak top as the energy loss, M was calculated as the energy loss separation between ^{41}Ca and ^{41}K. Moreover defined separation ability M' as $M' = M / (W_{Ca} + W_K)$, where W_{Ca} and W_K indicates the FWHM for respective section's energy loss. A maximum separation ability (M' = 2.2) at isobutane 24 Torr was obtained. In the cases of poor separation ($M' < 1.0$) ^{41}K entered the ^{41}Ca counting gate area, increasing the background level. The

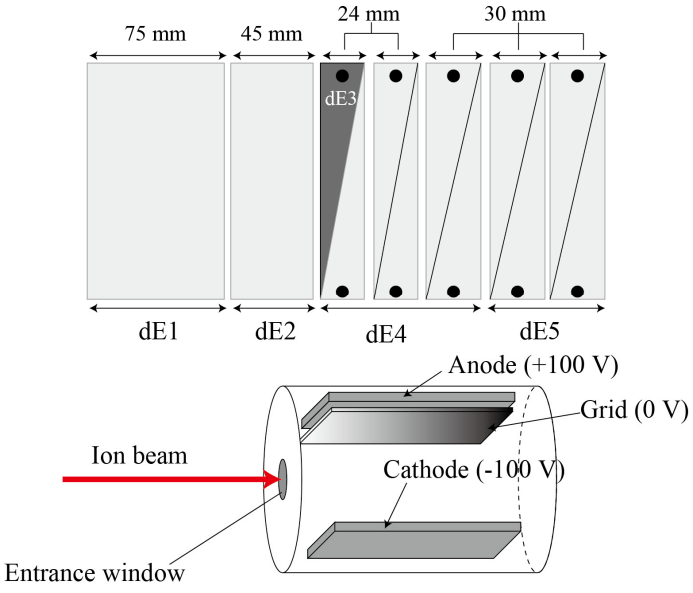

Fig. 1. Five-anode type ΔE-E detector.

[1] National Electrostatics Corporation, USA

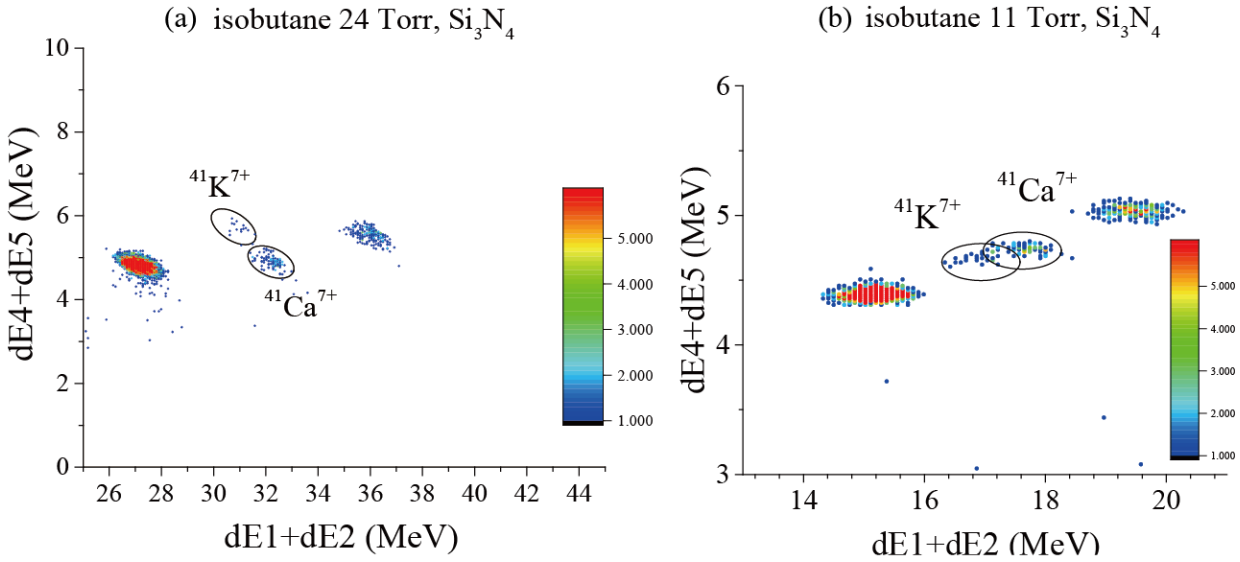

Fig. 2. ^{41}Ca AMS measured at different isobutane pressure: (a) 24 Torr and (b) 11 Torr. Separation ability *M'* is 2.2 in (a) and 0.9 in (b).

background level obviously decreased as the detector gas pressure increased, because there was no ^{41}K in the ^{41}Ca count gate area. We achieved a background level of ^{41}Ca/Ca ~ 6×10^{-14} at the best separation. Table 1 gives the characteristics of the ^{41}Ca AMS measurement at UTTAC. However, other facilities obtained lower backgrounds [5], [6], [7]. The CaF_3^- current in our case was ~ 100 nA, while other published values are ~ 300 nA [5], [6], [7]. It's pointing out that present measurement was as a test using the new 6 MV AMS system, therefore we think that higher CaF_3^- currents and consequently lower background measurements will be improved by adjusting the ion source and accelerator parameters.

Table 1. Characteristics of the ^{41}Ca AMS measurement by the new 6 MV AMS system at UTTAC.

Isotope	^{41}Ca
Target	CaF_2
Injected ion	CaF_3^-
Injectable ion current (nA)	~ 100
Transmission (%)	~ 5
Detected ion	$^{41}Ca^{7+}$
Stripper	Carbon foil (4.8 μg/cm^2)
Terminal voltage (MV)	6.0
Total energy (MeV)	44.5
Background level (^{41}Ca/^{40}Ca)	~ 6×10^{-14}

References

[1] Y. Nagashima et al., Nucl. Instr. Meth. Phys. Res. B 92 (1994) 55-57.
[2] K. Sasa et al., Nucl. Instr. Meth. Phys. Res. B 361 (2015) 124-128.
[3] D. Elmore et al., Nucl. Instr. Meth. Phys. Res. B 52 (1990) 531-535.
[4] T. Sato et. al., J. Nucl. Sci. Technol. 50 (2013) 913-923.
[5] K. Welten et al., Nucl. Instr. Meth. Phys. Res. B 259 (2007) 653-662.
[6] T. Schulze-Konig et al., Nucl. Instr. Meth. Phys. Res. B 268 (2010) 752-755.
[7] S. Akhmadaliev et al., Nucl. Instr. Meth. Phys. Res. B 294 (2013) 5-10.

3.3 Environmental impact of the Fukushima accident on iodine-129 levels in rainwater

M. Matsumura, K. Sasa, M. Watanabe[1], T. Matsunaka, T. Takahashi, K. Sueki, H. Matsuzaki[2]

In 2011, huge amounts of radionuclides were emitted into the atmosphere after the serious accident at the Fukushima Daiichi Nuclear Power Plant (FDNPP). Radioactive contaminations spread on the large terrestrial environment. Rainwater is a primary factor to precipitate atmospheric radionuclides over a long term. We have measured ^{129}I (half-life: 1.57×10^7 y) deposition in meteoric water samples collected before and after the FDNPP accident. The measurement was done by using an accelerator mass spectrometry (AMS) system at the Micro Analysis Laboratory Tandem Accelerator (MALT), The University of Tokyo[1]. The bulk precipitation samples were collected monthly at the University of Tsukuba[2], prepared from rainwater located about 170 km southwest of FDNPP.

The AMS results, shown in the Fig. 1, conclude that ^{129}I concentration in the rainwater before the accident was approximately 10^8 atoms L^{-1} at Tsukuba. On the other hand, ^{129}I concentration in March, 2011 was higher than that before the accident by approximately three orders of magnitude. It took approximately one year to return to the background level before the accident. This suggests that the atmospheric ^{129}I-radioactivity is a sensitive measure for the FDNPP accident. Also, the period of re-suspension suggesting atmospheric ^{129}I concentration and deposition caused by the FDNPP accident was approximately one year.

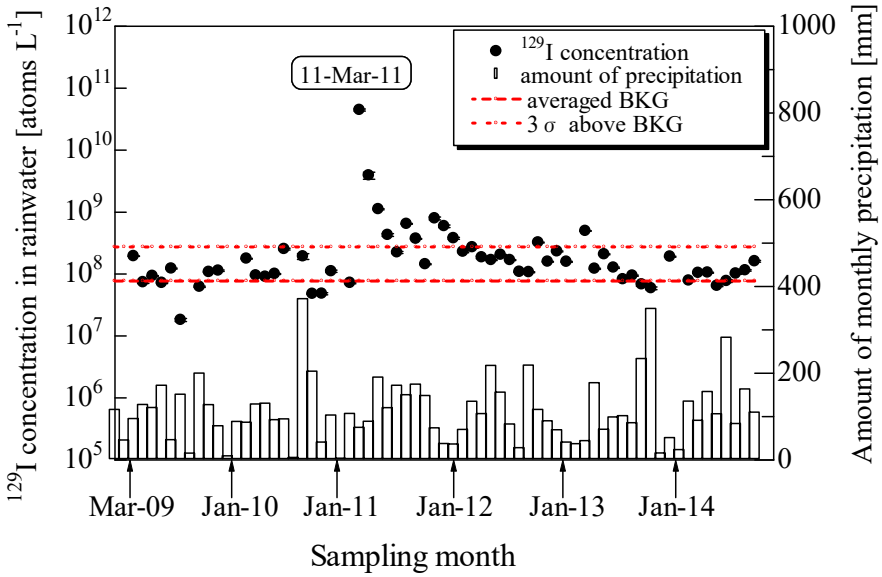

Fig. 1. The amount of precipitation and ^{129}I concentration in rainwater collected at University of Tsukuba.

References

[1] Matsuzaki et al., Nucl. Instr. Meth. Phys. Res. B 259 (2007) 721.

[2] Tosaki et al., J. Environ. Rad. 106 (2012) 73.

[1] Ehime Institute of Industrial Technology
[2] The University Museum, The University of Tokyo

3.4 Decrease of iodine isotopic ratio observed in the crater lake and the geothermal area at Zao volcano

T. Matsunaka, K. Sasa, K. Sueki, T. Takahashi, M. Matsumura, A. Goto[1], T. Watanabe[2], N. Tsuchiya[2], N. Hirano[2], M. Kuri[3], M. Takahashi[4], K. Kazahaya[4], I. Miyagi[4], H. Matsuzaki[5]

The volcanic activity has become higher at Zao volcano in Miyagi and Yamagata Prefectures of Japan since January 2013 after the 2011 Tohoku Earthquake. Monthly volcanic earthquakes of up to 319 times were observed in April 2015, and twice of the white turbidity were found on the surface of crater lake in October 2014 [1]. Basic water quality of crater lake and geothermal area have been studied by Tohoku University since the water quality of hydrothermal system in volcano has been confirmed to be correlated with the volcanic activity [2]. As a part of this investigation, we have tried to monitor the volcanic activity using $^{129}I/^{127}I$ ratios at Zao volcano. In our previous study, $^{129}I/^{127}I$ ratios in the water samples collected in October 2013 from the crater lake at Zao volcano were in the range of $1.6–2.2 \times 10^{-9}$, which were affected by anthropogenic meteoric water with high $^{129}I/^{127}I$ ratio ($> 9.0 \times 10^{-9}$) [3]. In terms of the global iodine cycle, chronologically-old iodine with low $^{129}I/^{127}I$ ratio ($< 1.5\times10^{-12}$ [4]) was considered to be supplied into the crater lake and geothermal area from underground corresponding to the volcanic activity, resulting the decrease in $^{129}I/^{127}I$ ratio of the crater lake. The present study aims to elucidate the relation between the $^{129}I/^{127}I$ ratio and volcanic earthquakes through the evaluation of $^{129}I/^{127}I$ ratio distribution in order to monitor volcanic activity at Zao volcano.

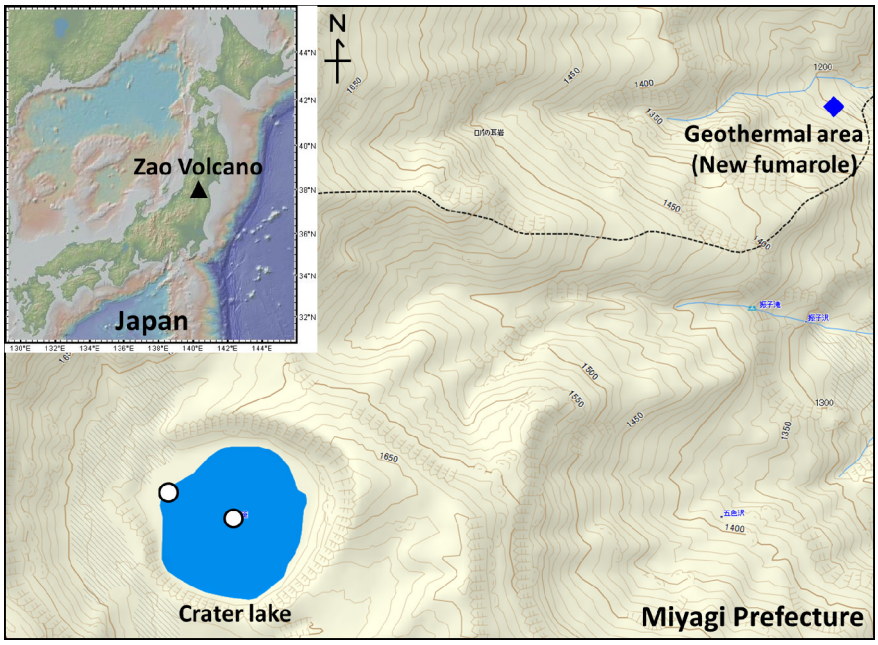

Fig.1. Map of Japan showing the location of Zao Volcano and sampling sites of water in the crater lake (white circles) and the geothermal area (blue diamond).

[1] Center for Northeast Asian Studies, Tohoku University
[2] Graduate school of Environmental Studies, Tohoku University
[3] International Research Institute of Disaster Science, Tohoku University
[4] Research Institute of Earthquake and Volcano Geology, AIST
[5] The University Museum, The University of Tokyo

Water samples (2000 ml) were collected 6−7 times from crater lake and geothermal area in eastern side of Zao volcano from October 2013 to October 2014 including before and after the white turbidity phenomena in the lake. After adding 2 mg iodine carrier to the filtered water sample of 1000 ml, the iodine was isolated and precipitated as AgI. The $^{129}I/^{127}I$ ratio of AgI target was measured using an accelerator mass spectrometry (AMS) system at the Micro Analysis Laboratory Tandem Accelerator (MALT), The University of Tokyo. A terminal voltage of 3.47 MV and a charge state of 5+ were chosen for acceleration and detection. Concentration of ^{127}I in the water was measured by an ICP-MS at the University of Tsukuba. The original $^{129}I/^{127}I$ ratios in the water samples were calculated using ^{127}I concentration and $^{129}I/^{127}I$ ratio.

The $^{129}I/^{127}I$ ratios of the crater lake increased from 2.2×10^{-9} to 5.6×10^{-9} during October 2013 to the middle of October 2014 corresponding to the decreased number of the volcanic earthquake, then, abruptly decreased to 4.3×10^{-10} soon after the white turbidity in the lake. While the $^{129}I/^{127}I$ ratios of the geothermal area decreased from 5.3×10^{-9} to 1.6×10^{-9} at August 2015 corresponding to the increased number of the volcanic earthquake. There is a possibility that the $^{129}I/^{127}I$ ratio in the crater lake is related to the volcanic activity at Zao volcano. Further investigations are needed to discuss the relationship of changes in $^{129}I/^{127}I$ ratio of the hydrothermal system and the volcanic activity at Zao volcano.

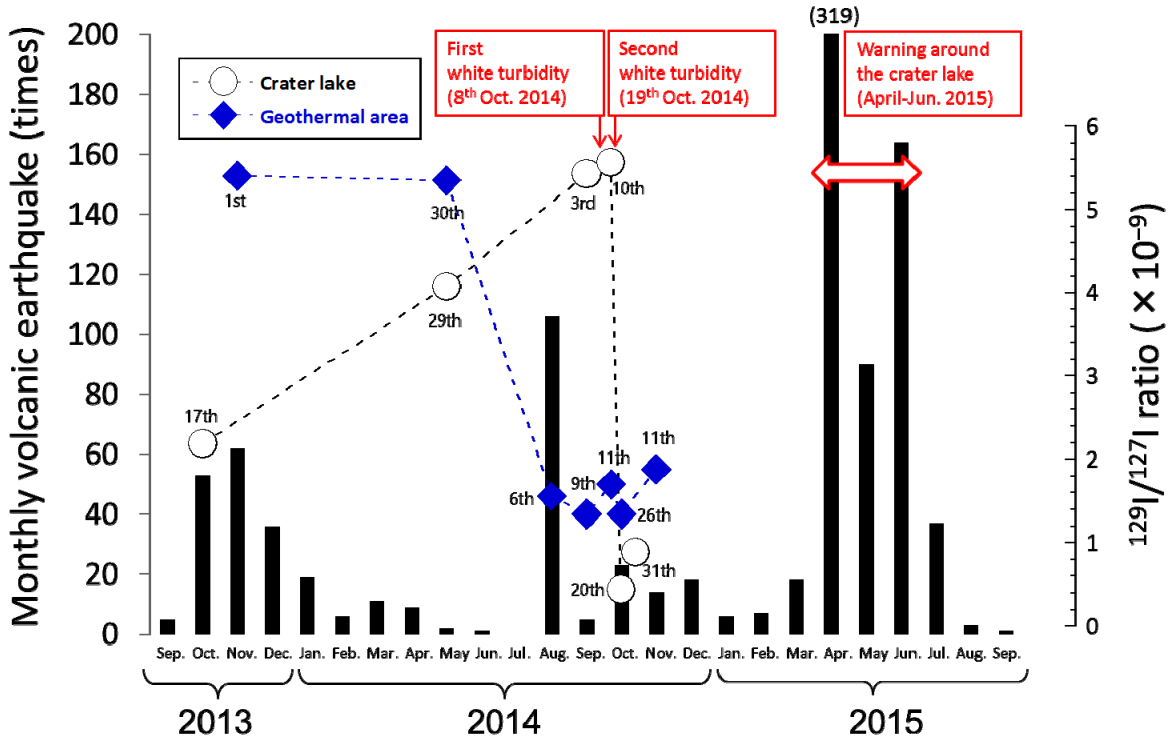

Fig.2. Number of monthly volcanic earthquake (black bars) at Zao volcano in 2013-2015. Also shown are the temporal changes in $^{129}I/^{127}I$ ratio of surface water from the crater lake (open circles) and the geothermal area (blue diamonds). The red remarks indicate the date of the white turbidity observed on the lake and the date of warning around the lake.

References

[1] Japan Meteorological Agency, Monthly Volcanic Activity Report (2015) (in Japanese).

[2] T. Ohba et al., J. Volcanol. Geotherm. Res. 178 (2008) 131–144.

[3] T. Matsunaka et al., KEK Proceedings 2015-4 (2015) 55–61.

[4] U. Fehn et al., Nucl. Instr. Meth. Phys. Res. B 259 (2007) 496–502.

4.

BEAM AND ISOTOPE APPLICATIONS

4.1 Micro-PIXE analyses of melt inclusions in olivine crystals from Allende meteorite

M. Kurosawa, D. Miyato, K. Sasa, S. Ishii

Introduction

Chondrules are millimeter-sized spherical particles consisting chiefly of olivine and pyroxene minerals embedded in matrices of primitive meteorites (chondrites) (Fig. 1a). They are thought to have been produced by the melting and sudden quenching of pre-existing silicate materials in the very early solar nebular before being accreted to their parent asteroids. They were formed at about 4564.7±0.6 million age (Ma) [1], about 2.5 Ma after the birth of the solar system (4567.4±0.6 Ma, [1]), within 5 astronomical unit (AU) from the proto-Sun as solidified melt droplets freely floating in space before the accretion [2]. They also constitute up to 80% of the volume of the most chondrites [3] that are believed to be the building blocks of the planetary system. Thus, an understanding of the formation of chondrules is important to elucidate the initial development of the early planetary system. Olivine crystals in chondrules usually contain tiny inclusions of Ca and Al-rich silicate glasses [2, 4-12] (Fig. 1b). The glasses have been generally regarded as small volumes of parental chondrule-melt trapped along olivine growth facets during chondrule formation [5-8, 12]. The chondrule melts are also thought to have reacted with the ambient nebular gas during the chondrule formation and to have incorporated the moderately volatile elements, Si, Fe, Cr, Mn, P, K, Na, Cl, Zn, and S from the nebular gas [2, 9-11, 13]. Thus, minerals and glass inclusions in chondrules are enriched in the moderately volatile elements [2, 9-11, 13]. Since the glass inclusions behave as a closed system during secondary alterations in their parent bodies [8-11], abundances of the moderately volatile elements in the inclusions are a clue to elucidate physico-chemical conditions in the early solar nebular gas and the chondrule formation processes. For the reason, we analyzed trace-element contents in glass inclusions from olivine crystals of Allende meteorite by using micro-PIXE.

Sample and Experimental

Allende meteorite is a carbonaceous chondrite classified as CV3 that is rich in refractory elements like Ca, Al, and Ti, and lacks secondary heating effects. The meteorite includes three types of olivine crystals: olivine phenocrysts in chondrules, isolated olivine crystals in the chondritic matrix, and irregular-shaped holocrystalline olivine aggregates in the matrix. In this study, glass inclusions in olivine phenocrysts from porphyritic olivine chondrules were analyzed. The glass inclusions were isolated or form clusters in the olivines. They were composed of

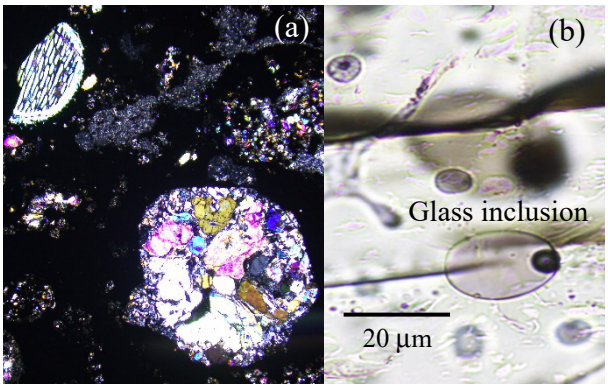

Fig.1. Photomicrographs of chondrules in Allende meteorite (a) and glass inclusions in olivine crystal within the chondrule (b). (a) Chondrules, bright parts of semicircular fragment (upper left) and spheroidal (lower right); matrix, dark area. (b) Ellipsoidal glass inclusions with transparent glass and dark shrinkage bubble.

clear glass plus shrinkage bubble (Fig. 1b) with sizes ranging from 5 to 30 μm. The surfaces of glass inclusions were exposed on surfaces of the olivine specimens by cutting and polishing and were coated with a carbon film to prevent electrostatic charging. Major element compositions of the glass inclusions were analyzed with a SEM-EDS prior to the PIXE analyses. The glass were rich in SiO_2 (50–61 wt%), Al_2O_3 (20–26 wt%), CaO (1.2–13.6 wt%) and have high contents of Na_2O (8.6 –13.1 wt%).

PIXE analyses were performed at the 1MV Tandetron. A 0.1 to 0.3 nA beam of 1.92-MeV proton was focused to a 10 × 10 μm spot on the sample using slits and magnetic lenses. The beam incidence was normal to the sample surface, and the X-ray measurement take-off angle was 45° [14]. The characteristic X-rays excited by the incident beam were collected by the Si(Li) X-ray-energy detector (Sirius 30+ detector; e2V Scientific Instruments, UK) with a nominal resolution of 139 eV at 5.9 keV. A 55-μm-thick Mylar film was used to attenuate the intense X-rays from the predominant light elements and to prevent the entry into the detector of protons scattered from samples. The total charge was determined by integrating the target currents, and all samples were analyzed to the integrated charges of 0.2 to 0.6 μC. Analytical points were chosen based on optical viewing using a CCD camera mounted on the microscope. Quantification was performed based on the model of Kurosawa et al. [14].

Results and Discussion

PIXE spectra of glass inclusions in the olivinecrystals consisted of K X-ray peaks from Ai, Si, Cl, K, Ca, Ti, Cr, Fe, Ni, Cu, Zn, and Sr (Fig. 2). All the glass inclusions in the olivines demonstrated the similar X-ray spectra. Element concentrations of the glass inclusions, determined by PIXE, were as follows: 22.7 to 25.9 wt.% for Si, 6.7–12.3 wt.% for Al, 3.4–9.8 wt.% for Ca, 0.2–1.1 wt.% for Fe, 0.22–0.47 wt.% for Ti and Cr, 180–9000 ppm for K and Ni, 600–960 ppm for S, and several tens to 400 ppm for P, Sc, Mn, V, Cl, Co, Cu, Sr, and Pb.

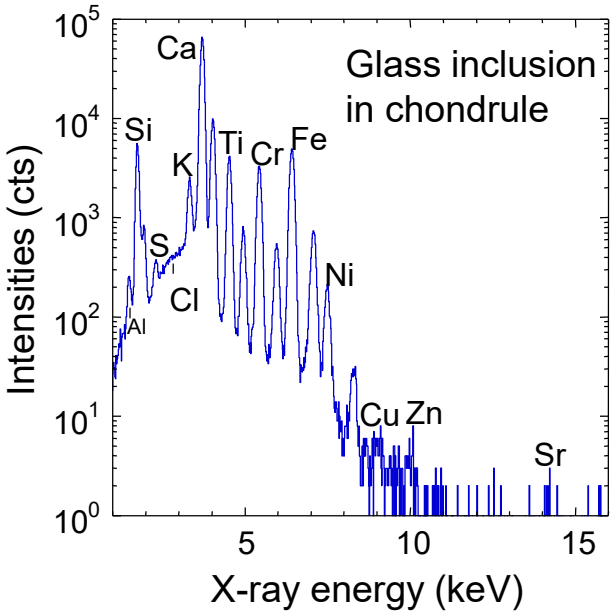

Fig.2. PIXE spectrum of glass inclusion in olivine crystal from Allende meteorite.

Contents of the refractory elements, Al, Ti, and Ca, were ten times higher than the solar- system abundances [15] and were comparable to those of glass inclusions from Kaba CV3 and Renazo CR2 carbonaceous chondrites [9, 10]. Contents of the moderately volatile elements, Si, V, and Cr were almost comparable to the solar-system abundances [15], and contents of S, Zn, and Cl were extremely lower than the solar-system abundances. Such volatility dependence agreed with those of glass inclusions from other carbonaceous chondrite [9, 10]. However, Na and K contents were extremely high contents, despite the moderately volatile elements. The high contents in the glass inclusions indicate their incorporations in extremely Na- and K-enriched conditions. Their moderately volatile elements may have been concentrated in the primordial nebular gas at the formation

regions of the Allende chondrite.

References

[1] Y. Amelin et al., Science 297 (2002) 1678.
[2] G. Libourel et al., Earth Planet. Sci. Lett. 251 (2006) 232.
[3] B. Zenda, Earth Planet. Sci. Lett. 224 (2004) 1.
[4] L. Fuchs et al., Smithson. Contrib. Earth Sci. 10 (1973) 38.
[5] H. McSween, Geochim. Cosmochim. Acta 41 (1977) 411.
[6] E. Roedder, Bull. Mineral. 104 (1981) 339.
[7] J. Makjanic et al., Meteoritics 24 (1989) 49.
[8] M. Varela et al., Geochim. Cosmochim. Acta 64 (2000) 342.
[9] M. Varela et al., Geochim. Cosmochim. Acta 66 (2002) 1663.
[10] M. Varela et al., Icarus 178 (2005) 553.
[11] M. Varela et al., Geochim. Cosmochim. Acta 72 (2008) 3170.
[12] F. Faure et al., Earth Planet. Sci. Lett. 319-320 (2012) 1.
[13] R. Hewins and B. Zenda, Meteorit. Planet. Sci. 47 (2012) 1120.
[14] M. Kurosawa et al., Nucl. Instr. Meth. Phys. Res. B 266 (2008) 3633.
[15] E. Anders and N. Grevesse, Geochim. Cosmochim. Acta 58 (1989) 3451.

4.2 Improvement of coincidence detection system of ion and secondary electron in HERDA

T. Tamura, I. Harayama, Y. Watahiki, S. Ishii, D. Sekiba

In the previous annual report (2014) [1], we reported the development of coincidence detection system for high-resolution elastic recoil detection analysis (HERDA) [2, 3] to reduce the background level correlated to the dark current in micro-channel plate (MCP) used as the position sensitive detectors (PSDs). In the system, the H^+ ion and secondary electron from the stopper foil are coincidently detected by PSD1 and PSD2, respectively as introduced by another group [4, 5]. We previously concluded that the dark current noise in the HERDA spectrum was significantly reduced down to ~ 2% of the original amount, meanwhile the signals of H^+ ion were also apparently suppressed down to ~ 10%. In the present report we describe the recent resolution of this problem of the signal reduction.

We noticed that the problem of the signal reduction is attributed to the system parameter in the electronics units named “Universal coincidence” shown in Fig. 1. In the previous system, the outputs from the “Dual Sum” and “Delay Amp3” were directly sent to “Universal coincidence”. However this “Universal coincidence” accepts only the TTL signal, so that, when the pulse height of one of the outputs from “Dual Sum” and “Delay Amp3” was lower than 3 V, “Universal coincidence” did not work. As a result, “Universal coincidence” often did not create the “gate” of ADC, even though the H^+ ion and secondary electron were detected by PSD1 and PSD2, respectively. This problem happens due to the non-fixed gain of the MCP. Now we put the “Timing SCA (single channel analyzer)” in front of the “Universal coincidence”, then all the signals can successfully open the gate of ADC.

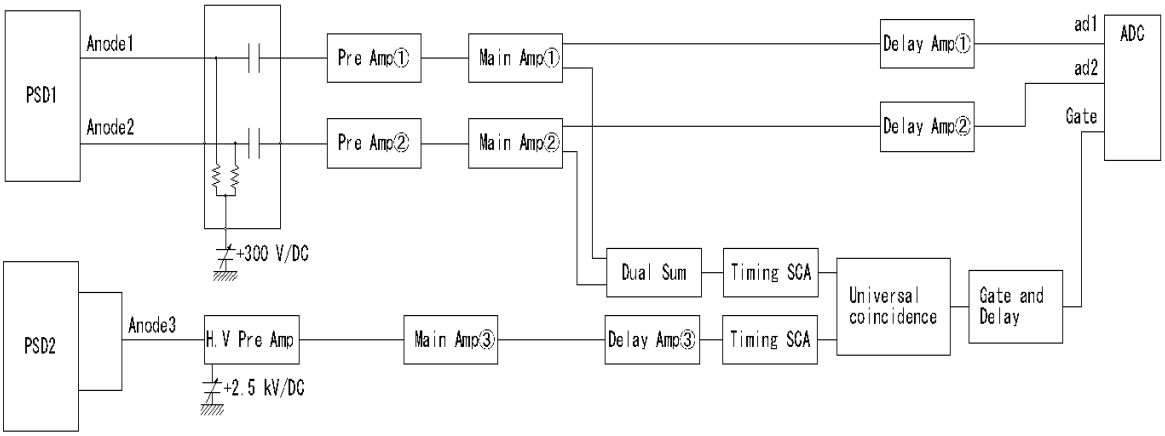

Fig.1. Schematics of data acquisition system in the coincidence detection system for HERDA.

The HERDA experiment with the new electronics was done at the D-course of 1MV Tandetron at UTTAC. The sample measured was hydrogenated amorphous carbon (a-C:H) film deposited on a Si wafer. The thickness of the a-C:H film is ~ 200 nm and chemical vapor deposition (CVD) was employed. The

500 keV $^{16}O^{+}$ ion was used as an incident beam, and the beam was shaped to 1 mm x 1 mm by a double slit system. The typical beam current was ~ 10 nA.

Figure 2 shows the HERDA spectra taken on the a-C:H film with (red) and without (blue) improved coincidence detection system. The yield of dark current (dotted lines) indicates that the dark current noise is reduced down to ~ 1%. The background at the vacuum region (70~90 ch) is also suppressed by the coincidence detection system. On the other hand, the reduction of the H+ ion yield (30~60 ch) due to the coincidence detection system is ~ 75%. This is much better than the previous value of ~ 10%. Taking into account the detection efficiency of MCP ~ 60%, 75% is very reasonable assuming that the H+ ion penetration induces emission of one or two secondary electrons. The difference between the background yield and the dark current yield with the coincidence detection system is interpreted by the multiple scattering of the incident beam.

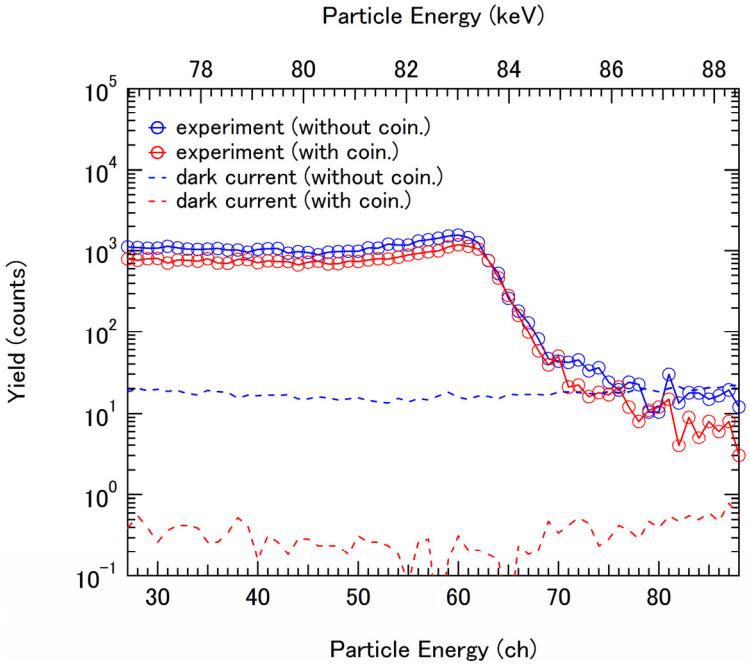

Fig. 2. HERDA spectra taken on the a-C:H film with (red) and without (blue) coincidence detection system. The dark current yield was measured without beam incidence.

References

[1] T. Tamura, I. Harayama, S. Maeda, S. Ishii, D. Sekiba, UTTAC annual report 2014.

[2] K. Kimura, K. Nakajima, H. Imura, Nucl. Instr. Meth. Phys. Res. B 140 (1998) 397-401.

[3] K. Kimura, M. Mannami, Nucl. Instr. Meth. Phys. Res. B 113 (1996) 270-274.

[4] H. Hashimoto, K. Nakajima, M. Suzuki, K. Sasakawa, K. Kimura, Rev. Sci. Instrum. 82 (2011) 063301.

[5] H. Hashimoto, S. Fujita, K. Nakajima, M. Suzuki, K. Sasakawa, K. Kimura, Nucl. Instr. Meth. Phys. Res. B 273 (2012) 241-244.

4.3 Vacancies in $In_xGa_{1-x}N$/GaN multiple quantum wells fabricated on *m*-plane GaN probed by a monoenergetic positron beam

A. Uedono, K. Kurihara[1], N. Yoshihara, S. Nagao[1], S. Ishibashi[2]

Vacancy-type defects in $In_xGa_{1-x}N$/GaN multiple quantum well (MQW) structures fabricated on *m*-plane GaN by metal organic chemical vapor deposition have been studied using a monoenergetic positron beam [1]. Through measurements of Doppler broadening spectra of the annihilation radiation, vacancy-type defects in MQW were probed. The positron trapping rate of defects decreased under photon illumination, which is attributed to the emission of electrons from those defects and/or the suppression of the positron diffusion by optically active defects. The energy level of the defects was close to the energy of photoluminescence emissions. The relationship between the energy width of the photoluminescence line and the defects is discussed. Results are shown in Figs. 1-5.

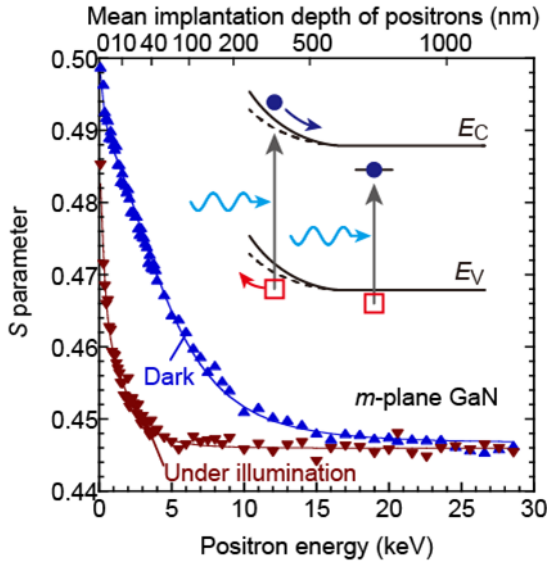

Fig. 1. *S* parameters as a function of incident positron energy *E* for *m*-plane GaN. The measurements were done in the dark (blue symbols) and under the illumination of HeCd-laser light (brown symbols). An inset shows a schematic band diagram for *n*-type semiconductor under illumination. A blue circle and a red square are an electron and a hole, respectively.

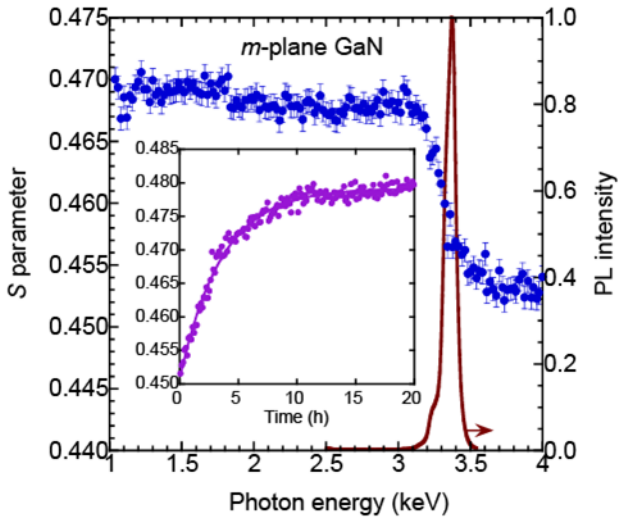

Fig. 2. Relationship between *S* and the photon energy for *m*-plane GaN. The PL spectrum is also shown. An inset shows the recovery of *S* after illumination with HeCd-laser light.

[1] Mitsubishi Chemical Corporation
[2] National Institute of Advanced Industrial Science and Technology (AIST),

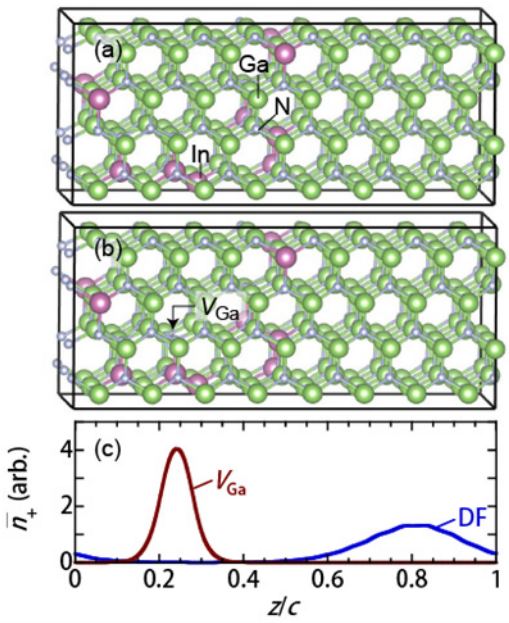

Fig. 3. (a) Atomic positions for the $In_{0.125}Ga_{0.725}N$/GaN heterostructure used in the calculations and (b) those with V_{Ga}, where purple, green, and gray spheres represent In, Ga, and N atoms, respectively. The planar averaged positron densities $\bar{n}_+$ corresponding to the defect-free structure (DF) and the structure with V_{Ga} are also shown in (c), respectively.

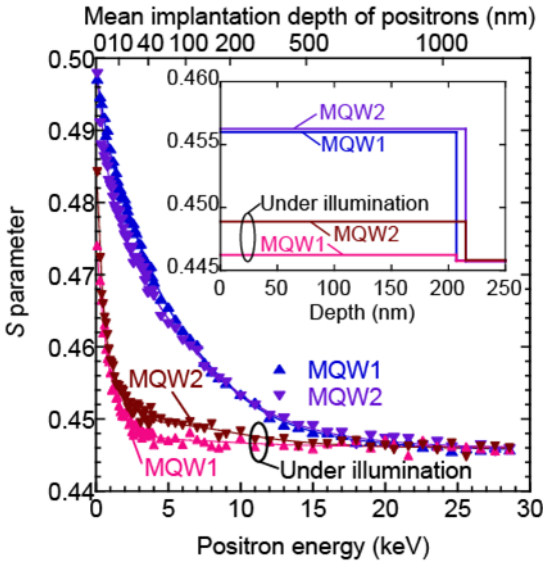

Fig. 4. *S*–*E* curves for the MQW1 and MQW2 measured in the dark (blue and violet symbols) and under the illumination of HeCd-laser light (pink and brown symbols). An inset shows the depth distributions of *S* derived from fittings.

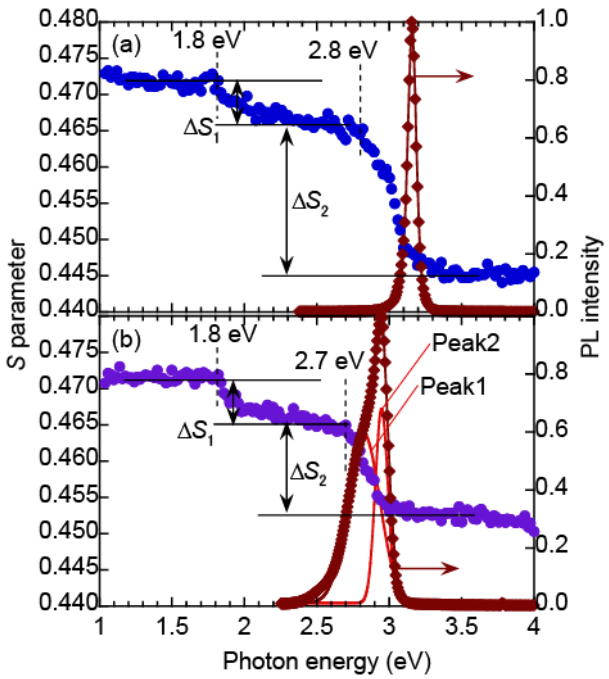

Fig. 5. Relationship between *S* and the photon energy for (a) MQW1 and (b) MQW2. The PL spectra are also shown.

Reference

[1] A. Uedono et al., Appl. Phys. Express 8 (2015) 051002.

4.4 Analysis of low Z elements in solids employing non-Rutherford backscattering

H. Naramoto, H. Kudo, M. Sataka, H. Oshima, K. Sasa, A. Uedono[1]

Interactions of fast ions with atoms in solids have been employed to perform the microstructural analysis of functional materials. The analytical information with the first priority in such a case is the depth distributions of relevant elements, which can be realized rather easily for heavy elements in low Z matrix by Rutherford backscattering spectrometry [1].

On the other hand, non-Rutherford process can be used to perform the sensitive analysis of low Z elements such as C, N and O in a surface-coating layer and/or compounds of functional materials [2, 3]. This can be realized advantageously, owing to the performance of the 6 MV tandem accelerator installed recently at UTTAC [4]. As the first step of this study, the energy calibration is performed employing the resonant nuclear elastic scattering $^{16}O(\alpha, \alpha_0)^{16}O$ around 3.04 MeV.

In non-Rutherford scattering, the differential cross sections of elastic scattering are strongly dependent on energy and scattering angle. Therefore, it is necessary in advance to perform the numerical approaches to such behavior of the cross sections. Figure 1 shows the numerically calculated excitation curves of $^{16}O(\alpha, \alpha_0)^{16}O$ nuclear elastic scattering at different scattering angles [5]. The peak energies are located at about 3.038 MeV. The peak increases from 140° up to 170°. One can realize the importance of a choice of scattering angle close to 170° where the cross section becomes larger by an order of magnitude compared with the Rutherford case.

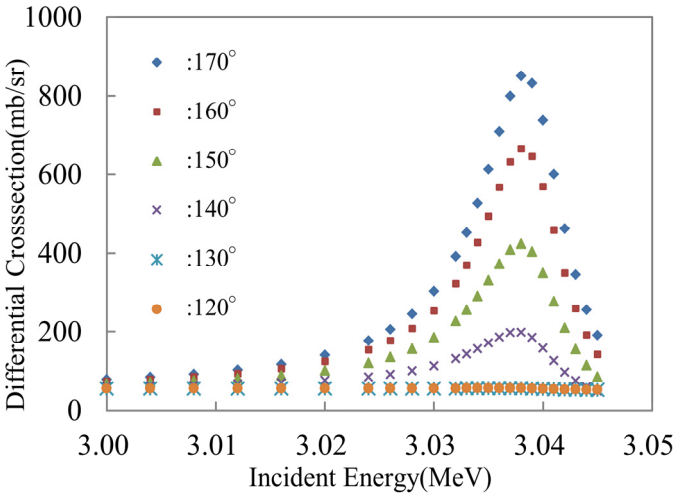

Fig. 1. The numerically calculated excitation curves of $^{16}O(\alpha, \alpha_0)^{16}O$ nuclear resonant scattering at six different backscattering angles.

For the energy calibration, naturally oxidized Al plate and single-crystalline α-Al_2O_3 were prepared. The energy of incident $^4He^{2+}$ ions (2 mmΦ in diameter, typically 10 nA) were changed across 3.040 MeV by small steps (5-20 keV/step), and the backscattered ^4He particles were detected with a surface barrier detector at a scattering angle of 168.5◦ over a solid angle of 2.76 msr.

Figure 2 shows the backscattering spectra from a naturally oxidized Al plate taken at 168.5◦ with different incident energies of $^4He^{2+}$ ions from 3.005 to 3.046 MeV. The thickness of oxidized layer is expected to be thin enough (several nm), so that the dependence of the resonance peak on the incident energy is drastic. The peak intensity shows the maximum at 3.045 MeV followed by the intensity drop at 3.046 MeV, which suggests that the resonant energy is around 3.045 MeV. For the quantitative evaluation,

[1] Also, Tsukuba Materials Research Co., Ltd.

α-Al_2O_3 single crystal with the fixed chemical composition was used as a standard sample. The energy width of incident $^4He^{2+}$ ions cannot be controlled to remain unchanged when changing the incident energies, and accordingly the resonance feature was observed as the peak shift in backscattering spectra.

Figure 3 shows the dependence of the peak energy on the incident energy for the resonant backscattering spectra. The flat top region around 1.192 MeV results from the convolution of resonant peaks all over the oxide layer, which includes the effect of energy struggling of incident $^4He^{2+}$ ions. The abrupt decrease of peak energy in the high energy region is caused by the energy loss of $^4He^{2+}$ ions backscattered deep inside. From Fig. 3, it is reasonable to take 3.044 MeV located at the middle in the flat region as the resonant energy. The resonance energy thus obtained, 3.044±0.002 MeV, is within the range of reported value [6].

This work has been carried out under the auspices of Open Advanced Facilities Initiative supported by Ministry of Education, Culture, Sports, Science and Technology, Japan.

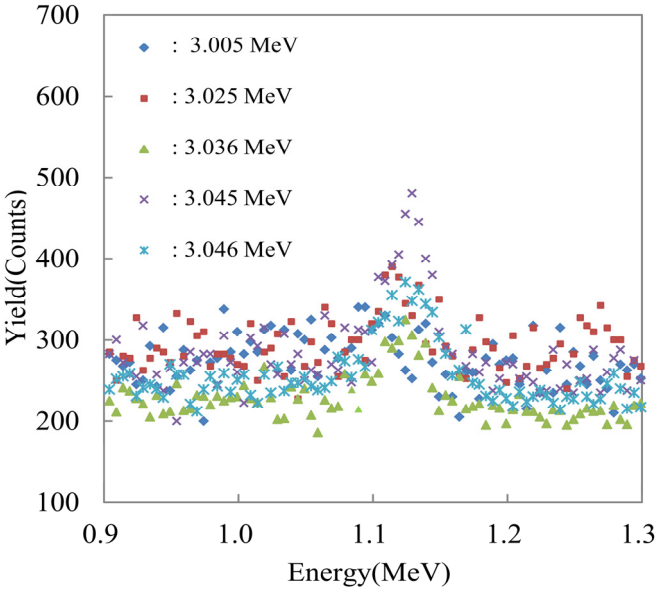

Fig. 2. Backscattering spectra of $^4He^{2+}$ ion from ^{16}O on naturally oxidized Al surface at 168.5° when the incident energy is changed from 3.005 MeV to 3.046 MeV.

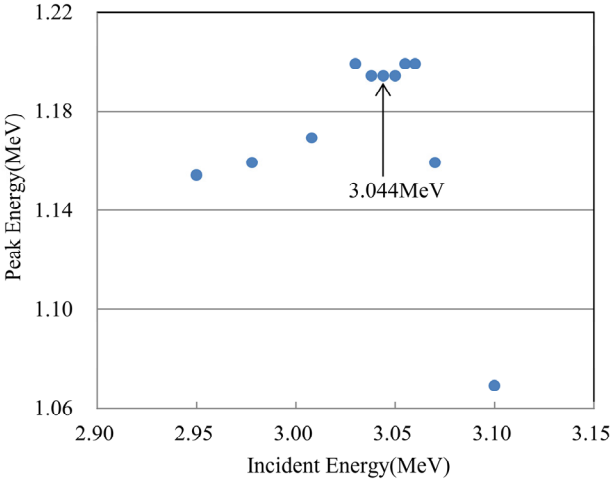

Fig. 3. The peak energy in resonant backscattering spectra of $^4He^{2+}$ ions in α-Al_2O_3 as a function of the incident energy. The arrow indicates the resonance energy determined in this work.

References

[1] W. K. Chu, J. W. Mayer, M-A. Nicolet, Backscattering Spectrometry, Academic Press, Inc. (1978).

[2] B. Blanpain, P. Revesz, L. R. Doolittle, K. H. Purser, J. M. Mayer, Nucl. Instr. Meth. Phys. Res. B 34 (1988) 459-464.

[3] W. Jiang, V. Shutthanandan, S. Thevuthasan, D. E. McCready, W. J. Weber, Nucl. Instr. Meth. Phys. Res. B 207 (2003) 453-461.

[4] K. Sasa, T. Takahashi, M. Matsumura, T. Matsunaka, Y. Satou, D. Izumi, K. Sueki, Nucl. Instr. Meth. Phys. Res. B 361 (2015) 124-128.

[5] A. F. Gurbich, Nucl. Instr. Meth. Phys. Res. B 371 (2016) 27-32.

[6] For example, V. I. Soroka, M. V. Artsimovich, I. Yu. Lobach, I, F. Moglnik. V. N. Tokarevsky, E. M. Kudriavtsev, B. N. Romanjuk, Nucl. Instr. Meth. Phys. Res. B 83 (1993) 311-318.

4.5 Performance of superconducting magnet for Mössbauer study (part 1)

S. Sharmin, H. Alima Latiff, H. Yanagihara, E. Kita

The Mössbauer effect is based on the principle that sometimes a nucleus in a solid matrix can emit and absorb gamma rays without recoil; this is because when it is in a solid matrix the nucleus is no longer isolated, but is fixed within the lattice. In general, the Mössbauer effect is optimized for low-energy gamma rays associated with nuclei strongly bound in a crystal lattice at low temperatures [1]. The applicability of superconducting magnets to studies of the Mössbauer effect stems from several factors. The fields obtainable are sufficiently large so as to produce useful magnetic hyperfine splittings by direct interaction with the nuclear magnetic moment. This permits the determination of nuclear magnetic moments even in nonmagnetic environments. Because the hyperfine fields are usually of the order of 40-50T, the external fields must often amount to several tesla, to resolve the spectra of the opposite magnetic moments in ferrimagnetic materials [2].

The magneto-optical system Spectromag (SM4000), an Oxford Instruments superconducting magnet capable of generating magnetic fields up to 6 T was set up in 2015-2016 at UTTAC for Mössbauer spectroscopic study purposes. The magnet is a so-called split-coil system, consisting of two Nb-Ti coils and a small cancellation coil. This coil produces a zero field at the location of the source. The goal of this design is to minimize the stray field while achieving the homogeneous high magnetic field required. In this configuration, the field is longitudinal, i.e. in the direction of the γ-rays. The whole magnet system is located in a cryostat with internal liquid helium and liquid N2 vessel. The split-pair superconducting magnet system provides optical access to a sample in a variable horizontal magnetic field and low temperature environment. A variable temperature insert (VTI) to allow for temperatures ranging from 0.45 to 300K with optical access was provided. The Spectromag is operated using a standard set of Oxford Instruments electronics and accessories:

i MercuryiPS-M superconducting magnet power supply
ii Mercury iTC temperature controller
iii ILM liquid helium/nitrogen level meter
iv flexible liquid helium transfer tube (siphon).

Fig.1. Setup of the measurement system with superconducting magnet.

Stray fields can seriously affect the normal measurements which are made to effect a velocity calibration of the spectrometer. In Fig. 2, the stray field distribution of the Spectromag has been presented. The numbers and arrows indicate the amplitude and direction of the stray fields in Oe units. The linear driver experiences magnetic field of 83 Oe when it is separated by 36 cm from the edge of the SCM at 50 kOe. Since the shift in the velocity is proportional to the strength of the stray field, the transducer was kept apart from the dewar. In addition, as a magnetic shield, soft steel sheets were placed between the dewar and the transducer.

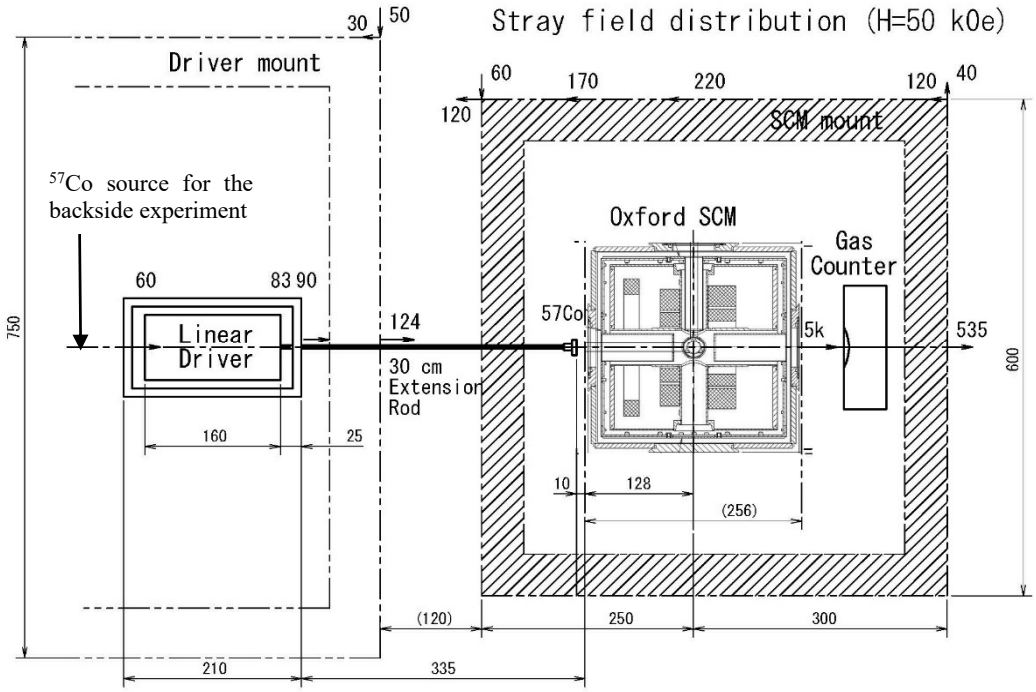

Fig. 2. Stray magnetic field distribution of the Oxford SPECTRO-MAG magnetized at 50 kOe. The numbers and arrows indicate the amplitude and direction of the stray fields in Oe units.

In order to populate the excited state of a Mössbauer isotope a radioactive isotope is needed which decays to its excited state. In the case of ^{57}Fe the radioactive isotope ^{57}Co is used. Also, ^{57}Fe(Rh) was used as a host throughout. The source can be attached to two vibrating systems (transducers) named LABO and WissEL, thus providing opportunity for two separate measurements to be conducted simultaneously. Liquid helium was provided by the Cryogenics Division, Research Facility Center for Science and Technology from recovered helium gas, transferred through a pipeline from the laboratory. After the sample was mounted in the sample space, the extension rod of the ^{57}Co source was attached to the drivers. The transmission of γ -rays was checked to see if there was about 20 counts/30 sec in each channel. After repeated evacuation of the sample space, outer vacuum jacket (OVJ), and VTI, the superconducting magnet was ready for use (see Fig. 1).

References

[1] D. P. E. Dickson, F. J. Berry, eds., Mössbauer Spectroscopy, Cambridge University Press (1986).

[2] W. Keune, Hyperfine Interactions 204 (2012) 13-45B.

4.6 Performance of superconducting magnet for Mössbauer study (part 2)

S. Sharmin, H. Alima Latiff, H. Yanagihara, E. Kita

Mössbauer spectroscopy under a high external magnetic field was performed in transmission geometry, in which the absorption of the γ-ray is detected. To evaluate the performance of the Mössbauer system with the superconducting magnet, a comparison of Mössbauer spectra for standard Fe (8 μm) with and without magnetic field was carried out. It was quite evident that the spectra change with the application of magnetic field, especially in the case of linewidth (LW), which increases as a magnetic field is applied (Fig. 1). Hyperfine field (H_{HF}) decreased from 330 kOe for H = 0 to 299 kOe under H = 50 kOe by about 30 kOe. The 2nd and 5th peaks disappeared due to the magnetization alignment parallel to the gamma-ray direction.

In order to double-check if the spectra really represent the Fe and exclude any experimental artifact, especially on the isomer shift (IS) and calibration factor, spectra of the α-Fe at the back side of the linear driver were also measured with the SCM charged at H = 0 and H = 5 T setting the another ^{57}Co source at the left side of the linear driver seen in Fig. 2 (secondary circuit side). These measurements directly test the effect of SCM magnetic field on the linear drive. Note that the α-Fe foil for the backside measurements was set with a distance of more than 60 cm from the SCM. Mössbauer spectra were shown in Fig. 2 and parameters are listed in Table 1. It was found that the linewidths for H=0 and H= 5 T were 0.32121 and 0.26247 mm/s respectively, almost equally opposite to the previous measurements where for H = 0 and H = 5 T the linewidths were 0.26057 and 0.33179 mm/s, respectively. If the system has the same velocity characteristics, then the calibration factors should not change. The calibration factor is 0.04586 for 5 T, which is almost the same as the zero field value, 0.04593. Therefore, we can say that the system characteristics remain the same and the effect of stray field from SCM on the driver is small.

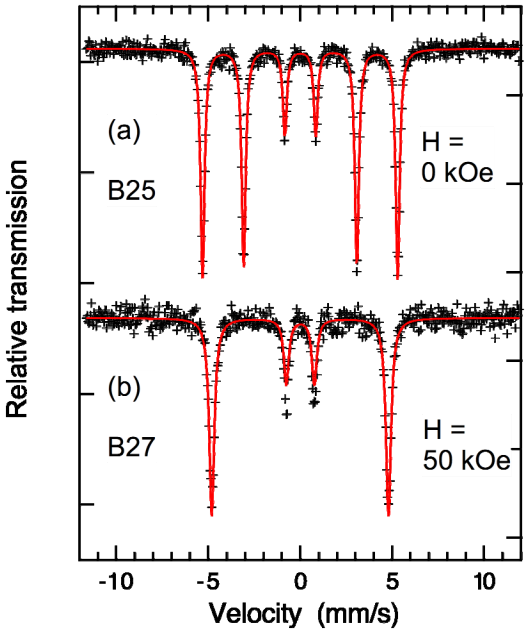

Fig.1. Mössbauer spectra of standard Fe (8 μm) at room temperature (a) H = 0 and (b) H = 50 kOe.

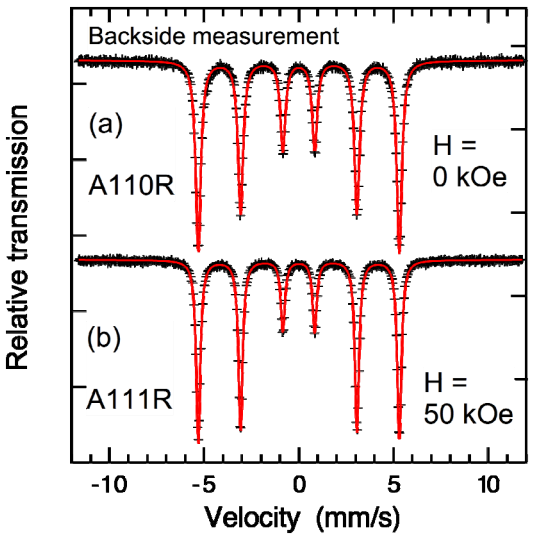

Fig.2. Mössbauer spectra of standard Fe (8 μm) measured at the backside, (a) H = 0 and (b) H = 50 kOe.

Table 1. Mössbauer parameters of standard Fe 8 μm absorbers measured under/near the external field (H) generated by the Oxford SCM system. Data were collected at room temperature and were analyzed as standard spectra where hyperfine field (H_{HF}) and isomer shift (IS) were fixed as 330 kOe and 0 mm/s, respectively, except spectrum recorded under 50 kOe.

	H (kOe)	H_{HF} (kOe)	IS (mm/s)	LW (mm/s)	Center Ch. (channel)	Cal fact. (mm/s/ch)	Exp ID		
SCM	0	330	-	0.26057	253.609	0.046012	B25	Std	Fig 3(a)
	50	298.86	0.0003	0.33179			B27		Fig 3(b)
Backside	0	330	-	0.32121	254.708	0.045925	A110R	Std	
	50	330		0.26247	254.674	0.045858	A111R	Std	

4.7 High magnetic field Mössbauer study on (Mg)Fe_3O_4 nano-particles

S. Sharmin, D. Isaka, H. Alima Latiff, M. Kishimoto, H. Yanagihara, E. Kita

Spinel ferrites exhibit various magnetic properties and have been utilized for many applications such as high and medium frequency power devices and signal transformers. The basic structure of spinel ferrite is magnetite, Fe_3O_4, with an inverse spinel structure where divalent ions are preferably placed on the B sites. Namely in magnetite, Fe^{3+} ions occupy A sites and equal amounts of Fe^{2+} and Fe^{3+} ions occupy the B sites of spinel structure. Magnetic structures are mainly determined by the strong antiferromagnetic interaction between A and B sites. Addition of metallic elements replacing divalent Fe^{2+} ions can modify the physical and magnetic properties. For example, Mn and Ni addition improve soft-magnetic properties and Zn addition can increase saturation magnetization. These features have been used for actual applications. Furthermore, novel applications have been developed for bio-medicine fields such as drug delivery and magnetic hyperthermia because ferrite oxides can realize biocompatible materials.

Magnetic nanoparticles of spinel oxides have attracted much attention because of their potential to generate heat in magnetic hyperthermia and thermoablation for cancer therapy. The origin of magnetically generated heat from inductive mediators essentially depends on the size and magnetic properties of the particles. Hysteresis loss is a dominant mechanism of heat generation for ferromagnetic and ferrimagnetic particles. We have been studying ferromagnetic nanoparticles, especially cobalt-doped magnetite particles, as high heat generating materials for magnetic hyperthermia and thermoablation. We must consider the biocompatibility of magnetic materials for their practical use. The biocompatibility of elements other than iron, cobalt in particular, must be carefully checked, even when they are used as dopants. Since cobalt toxicity is not fully understood, preparing cobalt-free particles is beneficial for safety aspects. We synthesized Mg-containing iron oxide particles and reported the basic characteristics of the (Mg)Fe_3O_4 particles [1]. The magnitude of the coercive forces peaked for the MTH1 sample and then decreased with increasing Mg content for the other samples.

Mössbauer measurements under an external magnetic field have been used to understand the charge-state distribution of magnetic ions in ferrimagnetic materials because magnetic fields work in different directions on Fe ions parallel and anti-parallel to an external field [2]. To understand the Mg ion distribution, which affect much on the magnetic properties, Mössbauer spectra were measured on the Mg introduced spinel ferrite nano-particles under the external magnetic field.

Spinel-structured Mg-containing iron oxide nanoparticles, (Mg)Fe_3O_4, were synthesized by co-precipitation and a hydrothermal process. We have labeled the various nanoparticle samples MTH0 through MTH6 corresponding to the increasing Mg content from 0 to 10.0 at% with respect to the total Fe content: the concentration of 2 at% in MTH1 corresponds to $Mg_{0.06}Fe_{2.94}O_4$. Characterization of the sample was summarized in the previous report [1]. ^{57}Fe Mössbauer spectra for the MTH1 sample were recorded at room temperature under 0 kOe and 40 kOe of the external magnetic fields. The spectra were numerically analyzed using commercially available fitting software, MössWinn 4.0.

The Mössbauer spectra recorded at room temperature are shown in Fig. 1. The spectrum without

magnetic field (H=0) can fit the combination of two magnetic sub-spectrum with almost the same parameters as Fe_3O_4. It is reasonable because only 2 % of Fe was replaced by Mg in the sample. The sub-spectrum with higher hyperfine field corresponds to Fe^{3+} on the A sites and the one with lower hyperfine field corresponds to $Fe^{2.5+}$ on the B sites. Under the magnetic field of 40 kOe, the spectrum is obviously composed of 3 sub-spectra. The sub-spectrum with highest hyperfine field should correspond to Fe^{3+} on the A site. However the other two sub-spectra cannot be understood simply and need to be analyzed carefully.

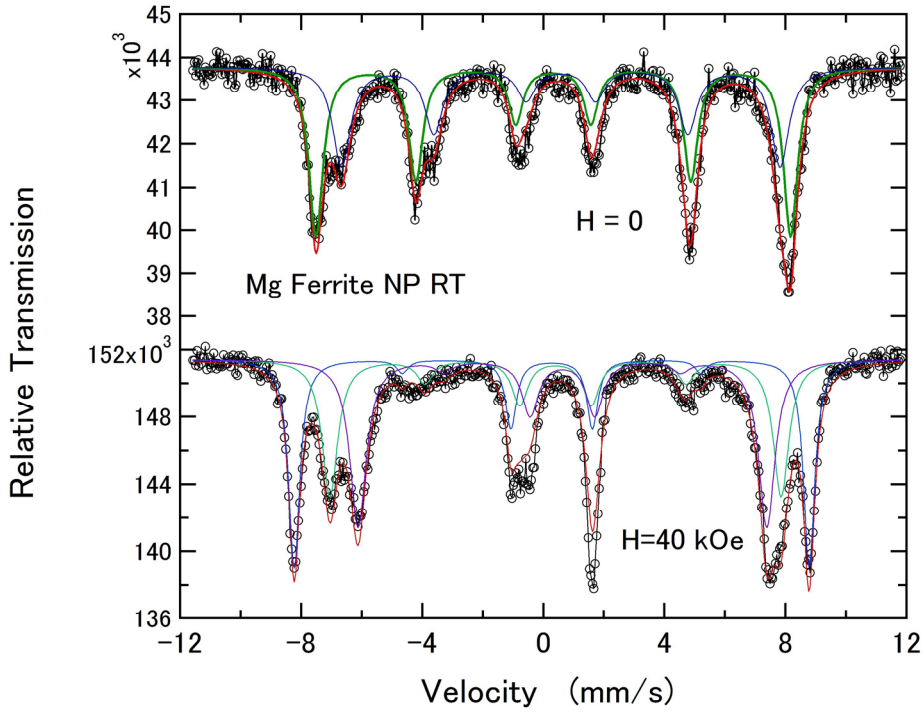

Fig. 1. Mössbauer spectra for $Mg_{0.06}Fe_{2.94}O_4$ nano-particles(NP) MTH1 measured at room temperature under no magnetic field (upper) and 40 kOe (lower).

References

[1] D. Isaka, M. Kishimoto, H. Yanagihara, E. Kita, UTTAC Annual report 2012 (2013) 28.

[2] J. Chappert, R.B. Frankel, Phys. Rev. Lett. 19 (1967) 570.

4.8 Effect of annealing temperatures on crystal structure of $CuFe_2O_4$ nanoparticles studied with Mössbauer spectroscopy

Hawa Latiff, M. Kishimoto, S. Sharmin, H. Yanagihara, E. Kita

Among all the spinel ferrites, cobalt ferrite (CFO) can exhibit extraordinarily large anisotropy when tetragonal distortion is introduced in the structure. In a previous study, we reported extraordinarily large perpendicular magnetic anisotropy in epitaxially strained CFO (001) thin films with K_u of almost 10 Merg/cm^3 by introducing a tetragonal distortion (c/a<1) [1]. Substrate-induced epitaxial distortion is controlled by the lattice constant mismatch of the substrate and the target. However, this type of distortion is only possible in thin films form of structure. In order for bulk production to be feasible, we propose the introduction of Jahn-Teller (JT) distortion in the nanoparticle structure. A typical example of the JT effect in spinel ferrite, is the tetragonal phase transformation of copper ferrite ($CuFe_2O_4$) observed at room temperature. In this report, $CuFe_2O_4$ particles were synthesized and the crystal structures were analyzed using Mössbauer spectroscopy.

$CuFe_2O_4$ particles were synthesized by coprecipitation and flux methods. Aqueous solutions containing Cu^{2+}, Fe^{2+}, and Fe^{3+} were mixed with NaOH aqueous solution to form precipitates. The precipitates were mixed with KBr flux, and heated at 850℃ for 3 hours. The particles obtained in this way were then rinsed with water a few times to remove the flux. Finally, the particles were annealed at 700–900°C for 2 h in air and/or in vacuum to investigate effect of annealing conditions on the crystal structure.

The XRD patterns of the samples, CF1, CFH1, CFH2, CFH3, CFH4, are shown in Fig. 1. For the as-fluxed particles (CF1) most of the peaks are of cubic spinel with a slight trace of peaks attributable to CuO. When the CF1 particles were heated to 700–800°C in air, peaks splitting are observed showing the mixed phase of cubic and tetragonal $CuFe_2O_4$. After heating at 900°C in air, a single phase tetragonal $CuFe_2O_4$ was obtained. On the other hand, when annealing treatment was carried out in vacuum environment, a cubic structure with fairly narrow line width was obtained. CFH4 has good crystallinity and no tetragonal distortion was confirmed from the XRD pattern.

^{57}Fe Mössbauer study was performed on CF1, CFH3 and CFH4 samples. The Mössbauer spectra recorded at room temperature are shown in Fig. 2 and the fitting parameters are tabulated in Table 1. Each spectrum was fitted to a combination of 1 or 2 sextets and/or 2 paramagnetic components. The values of $H_{h.f.}$, *I.S.*, *Q.S.*, and *L.W.* of bulk $CuFe_2O_4$ for both cubic and tetragonal phase were compared with published results by Evans *et* al. [2]. Sample CF1 had a wide line width and the Fe^{3+} originated spectrum was unresolved for A and B sites. The $H_{h.f.}$ value is somewhat larger, whereas the line width is almost the same as the bulk value.

The magnetic properties for sample CF1, CFH3 and CFH4 are summarized in Table 2. The saturation magnetization for CF1 and CFH3 were about the same as that of a complete inverse spinel (M_S ~21

emu/g). For CFH4, the value of M_S is about double the theoretical value, which suggests that it may contain 10% of normal spinel (M_S ~210 emu/g).

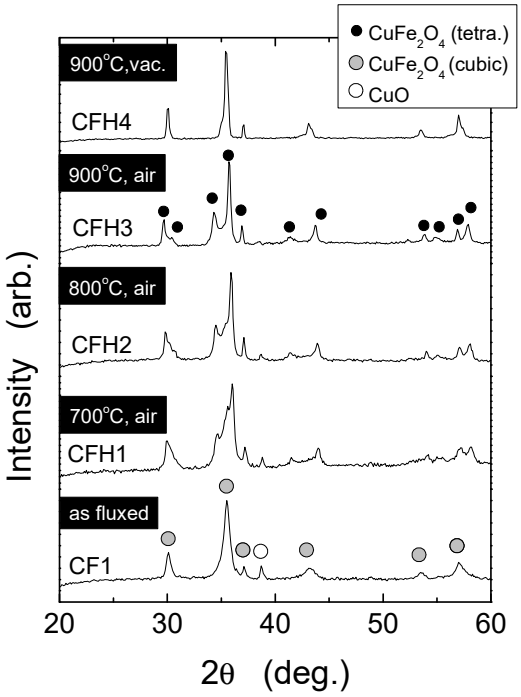

Fig. 1. XRD patterns of $CuFe_2O_4$ after annealing treatment at increasing temperature in air and/or vacuum.

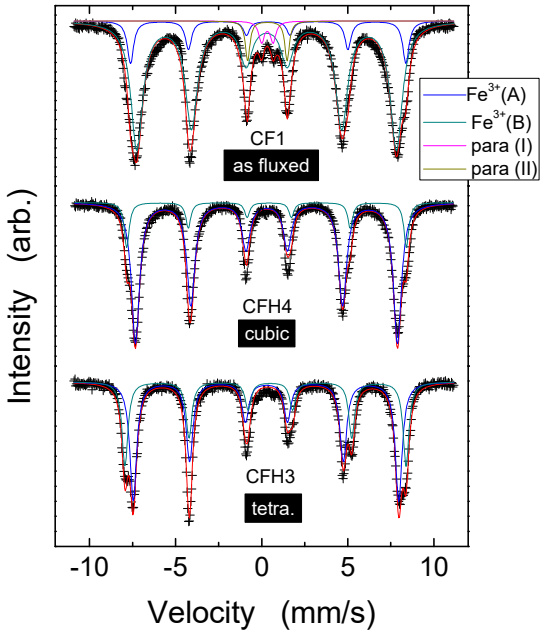

Fig. 2. Room temperature ^{57}Fe Mössbauer spectra of cubic and tetragonal $CuFe_2O_4$ particles.

Table 1. Mössbauer fitting parameters for spectra in Fig. 2.

Sample	XRD structure	Fit	$H_{h.f.}$ (T)	I. S. (mm/s)	Q. S. (mm/s)	L. W. (mm/s)	Area (%)
CF1	Cubic	Fe^{3+} (A, B)	50.8	0.30	-0.04	1.0	92.76
		Doublet (1)	-	0.35	0.70	0.38	2.40
		Doublet (2)	-	0.35	2.5	0.34	4.83
CFH4	Cubic	Fe^{3+} (A)	47.31	0.29	-0.015	0.57	84.61
		Fe^{3+} (B)	50.49	0.36	-0.158	0.35	15.39
CFH3	Tetragonal	Fe^{3+} (A)	47.94	0.27	-0.027	0.47	61.85
		Fe^{3+} (B)	50.76	0.36	-0.282	0.41	38.15

Table 2. Magnetic properties of the CF1, CFH3 and CFH4.

Sample	Structure (XRD)	D_{XRD} (nm)	M_S (emu/g)	H_C (Oe)
CF1	Cubic	13	25	133
CFH3	Tetragonal	36	26.9	823
CFH4	Cubic	66	41.2	57

References

[1] T. Niizeki et al., Appl. Phys. Lett. 103 (2013) 162407.

[2] B. J. Evans et al., J. Phys. Chem. Solid. 29 (1968) 1573.

4.9 PIXE measurements for light elements in inorganic materials by a silicon drift detector with a thin Si_3N_4 window

A. Yamazaki, K. Sasa, S. Ishii, M. Kurosawa, S. Tomita, A. Uedono, E. Kita

Light elements such as boron, nitrogen, and oxygen often play important roles in various characteristics of materials. Accordingly, instruments and methods for observing the light elements are indispensable for materials research. Better detection sensitivity is strongly required for these methods when a trace of light elements involved in a material is of physical and essential importance.

Particle induced X-ray emission (PIXE) is one of useful methods for elemental analysis using an ion beam and is suitable for detecting trace elements because of its relatively large emission cross section of inner-shell characteristic X-rays. In addition, PIXE provides data with high signal-to-background ratio because the intensity of the projectile bremsstrahlung, which is one of the causes of the continuous background, is much less than that induced by electron beams.

In these days, silicon drift detectors (SDDs) are often used for observing characteristic X-rays because the mounted silicon photodiode with ring electrodes enables high-count-rate measurements. However, it is difficult to detect the low-energy characteristic X-rays from light elements, which is not only for SDDs but also ordinary X-ray detectors such as Si(Li) detectors.

In UTTAC, SDD with a thin window is adopted to observe characteristic X-rays emitted from light elements in the structural materials. The front entrance window is made of silicon nitride (Si_3N_4) film coated with aluminum. The thicknesses of the Si_3N_4 film and the Al coating are 40 and 30 nm, respectively. Photographs of SDD, XR-100FastSDD (Amptek Inc., US) with pulse processing unit and its front window are shown in Fig. 1.

In order to examine the performance of the detection of low energy X-rays of several hundred keV, PIXE measurements were performed at the 1MV Tandetron facility. A 1.92 MeV proton beam was provided from the Tandetron accelerator and transported to the C course. A boron nitride (BN) plate and a Kapton film were placed at the center of the chamber and irradiated by the proton beam. In the vacuum chamber, SDD was placed at an angle of 150° with respect to the beam axis and observed X-rays emitted from the sample. The distance from the target and SDD was 95 mm and the solid angle of the SDD was 2.2 msr. The typical beam current was 37 pA on target.

Examples of the X-ray energy spectra obtained are shown in Fig. 2. The data accumulation time was about 20 minutes. The characteristic X-rays of boron (183 eV), carbon (277 eV), nitrogen (392 eV), and oxygen (525 eV), are clearly shown in Fig. 2. The FWHM of the carbon peak in the Kapton spectrum was about 66 eV. It should be noted that the spectra below 100 eV are cut off to prevent enormous electronic noises from coming into ADC. Suppression of the noises is strongly required for observing characteristic X-rays emitted from light elements, especially from boron.

Acknowledgement

This work is supported by Cross-ministerial Strategic Innovation Promotion Program - Unit D66 - Innovative measurement and analysis for structural materials (SIP-IMASM) operated by the cabinet office.

Fig. 1. Photographs of the silicon drift detector XR-100FastSDD with digital pulse processor (Amptek Inc., US) (left). An entrance window is made of silicon nitride (Si_3N_4) with a thickness of 40 nm for observing characteristic X-rays from light elements (right).

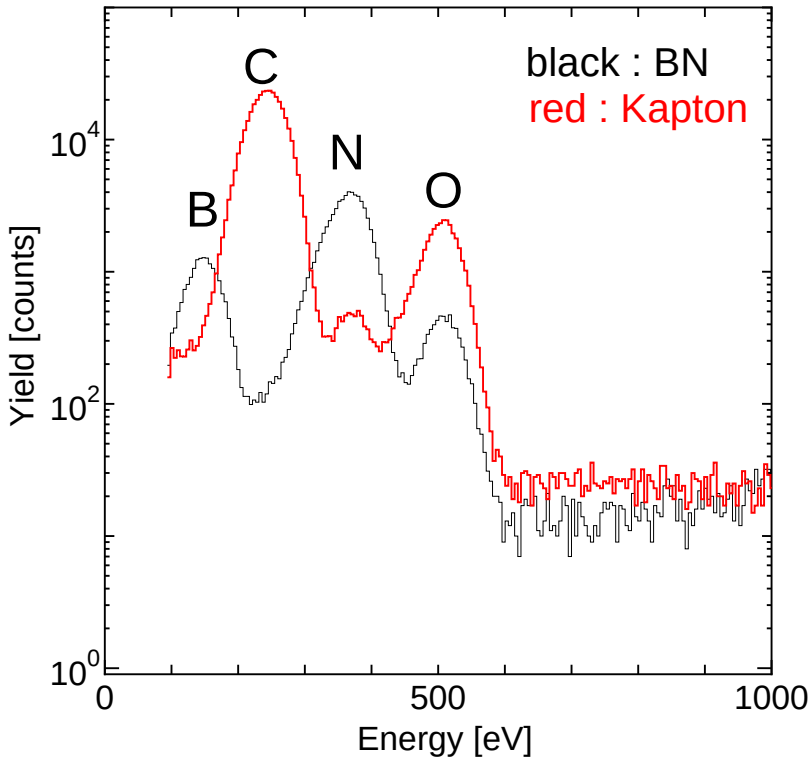

Fig. 2. X-ray energy spectra obtained by SDD with a thin silicon nitride (Si_3N_4) window.

5.

LIST OF PUBLICATIONS

5.1 Journals

ACCELERATOR AND EXPERIMENTAL FACILITIES

1. K. Sasa, T. Takahashi, M. Matsumura, T. Matsunaka, Y. Satou, D. Izumi, K. Sueki, "The new 6 MV multi-nuclide AMS facility at the University of Tsukuba", Nuclear Instruments and Methods in Physics Research B 361 (2015) 124-128.

NUCLEAR PHYSICS

1. Y. G. Ma, D. Q. Fang, X. Y. Sun, P. Zhou, Y. Togano, N. Aoi, H. Baba, X.Z. Cai, X. G. Cao, J. G. Chen, Y. Fu, W. Guo, Y. Hara, T. Honda, Z. G. Hu, K. Ieki, Y. Ishibashi, Y. Ito, N. Iwasa, S. Kanno, T. Kawabata, H. Kimura, Y. Kondo, K. Kurita, M. Kurokawa, T. Moriguchi, H. Murakami, H. Ooishi, K. Okada, S. Ota, A. Ozawa, H. Sakurai, S. Shimoura, R. Shioda, E. Takeshita, S. Takeuchi, W.D. Tian, H.W. Wang, J.S. Wang, M. Wang, K. Yamada, Y. Yamada, Y. Yasuda, K. Yoneda, G.Q. Zhang, and T. Motobayashi, "Different mechanism of two-proton emission from proton-rich nuclei ^{23}Al and ^{22}Mg", Physics Letters B 743 (2015) 306–309.

2. S. Omika, T. Yamaguchi, M. Fukuda, A. Kitagawa, S. Matsunaga, D. Nagae, D. Nishimura, T. Nishimura, A. Ozawa, S. Sato, K. Sawahata, T. Suzuki, and Y. Takeuchi, "Spatial distributions of photons in plastic scintillator detected by multi-anode photomultiplier for heavy-ion position determination" Nuclear Instruments and Methods in Physics Research A 797 (2015) 247–254.

3. S. Momota, I. Tanihata, A. Ozawa, M. Notani, K. Yoshida, K. Morimoto, T. Yamaguchi, T. Onishi, A. Yoshida, Y. X. Watanabe, Z. Liu, and A. Ono, "Velocity-dependent transverse momentum distribution of fragments produced from ^{40}Ar+^{9}Be at 95 MeV/nucleon", Physical Review C 92 (2015) 024608.

4. Y. Abe, Y. Yamaguchi, M. Wakasugi, T. Uesaka, A. Ozawa, F. Suzaki, D. Nagae, H. Miura, T. Yamaguchi and Y. Yano, "Isochronous field study of the Rare-RI Ring" Physica Scripta T166, 2015 (2015) 014047.

5. Y. Yamaguchi, H. Miura, M. Wakasugi, Y. Abe, A. Ozawa, F. Suzaki, A. Tokuchi, T. Uesaka, T. Yamaguchi and Y. Yano, "Fast-kicker system for rare-RI ring" Physica Scripta T166, 2015 (2015) 014056.

6. F. Suzaki, Y. Abe, A. Ozawa, T. Suzuki, T. Uesaka, M. Wakasugi, K. Yamada, T. Yamaguchi, Y. Yamaguchi, J. Zenihiro and the rare-RI Ring collaboration, "A resonant Schottky pick-up for Rare-RI Ring at RIKEN", Physica Scripta T166, 2015 (2015) 014059.

ACCELERATOR MASS SPECTROMETRY

1. T. Matsunaka, K. Sasa, K. Sueki, T. Takahashi, M. Matsumura, Y. Satou, J. Kitagawa, N. Kinoshita, H. Matsuzaki, "Pre- and post-accident ^{129}I and ^{137}Cs levels, and $^{129}I/^{127}I$ and $^{129}I/^{137}Cs$ ratios in soil profiles near the Fukushima Dai-ichi Nuclear Power Plant, Japan", Journal of Environmental Radioactivity 151 (2015) 209-217.

2. Y. Miyake, H. Matsuzaki, K. Sasa, T. Takahashi, "Measurement of long-lived radionuclides in surface soil around F1NPP accident site by Accelerator Mass Spectrometry", Nuclear Instruments and Methods in Physics Research B 361 (2015) 627-631.

3. Y. Satou, K. Sueki, K. Sasa, T. Matsunaka, T. Takahashi, N. Shibayama, D. Izumi, N. Kinoshita, H. Matsuzaki, "Technological developments for strontium-90 determination using AMS", Nuclear Instruments and Methods in Physics Research B 361 (2015) 233-236.

4. J. B. Wang, L. P. Zhu, Y. Wang, P. Peng, Q. F. Ma, T. Haberzettl, T. Kasper, T. Matsunaka, and T. Nakamura, "Variability of the ^{14}C reservoir effects in Lake Tangra Yumco, Central Tibet (China), determined from recent sedimentation rates and dating of plant fossils", Quaternary International 2015 (in Press) doi:10.1016/j.quaint.2015.10.084 (2016).

BEAM AND ISOTOPE APPLICATIONS

1. M. Kurosawa, K. Sasa, K. C. Shin, S. Ishii, Trace-element compositions and Br/Cl ratios of fluid inclusions in the Tsushima granite, Japan: Significance for formation of granite-derived fluids, Geochimica et Cosmochimica Acta 182 (2016) 216–239.

2. S. Tomita, Y. Nakai, S. Funada, H. Tanikawa, I. Harayama, H. Kobara, K. Sasa, J. O. P. Pedersen and P. Hvelplund, "Oxidation of SO_2 and Formation of Water Droplets under Irradiation of 20 MeV protons in $N_2/H_2O/SO_2$", Nuclear Instruments and Methods in Physics Research B 365 (2015) 616-621.

3. A. Uedono, M. Malinverni, D. Martin, H. Okumura, S. Ishibashi, and N. Grandjean, "Vacancy-type defects in Mg-doped GaN grown by ammonia-based molecular beam epitaxy probed using a monoenergetic positron beam", J. Appl. Phys. 119 (2016) 245702 (1-6). [DOI: 10.1063/1.4954288]

4. A. Uedono, Y. Tsukada, Y. Mikawa, T. Mochizuki, H. Fujisawa, H. Ikeda, K. Kurihara, K. Fujito, S. Terada, S. Ishibashi, and S. F. Chichibu, "Vacancies and electron trapping centers in acidic

ammonothermal GaN probed by a monoenergetic positron beam", J. Cryst. Growth 448 (2016) 117-121. [DOI: 10.1016/j.jcrysgro.2016.05.015]

5. W. Zhu, B. Mitchell, D. Timmerman, A. Uedono, A. Koizumi, and Y. Fujiwara, "Enhanced photo/electroluminescence properties of Eu-doped GaN through optimization of the growth temperature and Eu related defect environment", APL Mater. 4 (2016) 056103(1-7). [doi: http://dx.doi.org/10.1063/1.4950826]

6. S. Hooda, S. A. Khan, B. Satpati, A. Uedono, S. Sellaiyan, K. Asokan, D. Kanjilal, and D. Kabiraj, "Nanopores formation and shape evolution in Ge during intense ionizing irradiation", Microporous and Mesoporous Mat., 225 (2016) 323-330. [doi:10.1016/j.micromeso.2016.01.006]

7. A. Uedono, M. M. Islam, T. Sakurai, C. Hugenschmidt, W. Egger, R. Scheer, R. Krause-Rehberg, and K. Akimoto, "Vacancy behavior in $Cu(In_{1-x}Ga_x)Se_2$ layers grown by a three-stage coevaporation process probed by monoenergetic positron beams", Thin Solid Films 603 (2016) 418-423. [DOI: 10.1016/j.tsf.2016.02.057]

8. K. Kojima, Y. Tsukada, E. Furukawa, M. Saito, Y. Mikawa, S. Kubo, H. Ikeda, K. Fujito, A. Uedono, and S. F. Chichibu, "Electronic and optical characteristics of an m-plane GaN single crystal grown by hydride vapor phase epitaxy on a GaN seed synthesized by the ammonothermal method using an acidic mineralizer", Jpn. J. Appl. Phys. 55 (2016) 05FA03(1-4). [DOI: 10.7567/JJAP.55.05FA03]

9. A. Uedono, S. Armini, Y. Zhang, T. Kakizaki, R. Krause-Rehberg, W. Anwand, and A. Wagner, "Surface sealing using self-assembled monolayers and its effect on metal diffusion in porous low-k dielectrics studied using monoenergetic positron beams", Appl. Surf. Sci. 368 (2016) 272-276. [DOI:10.1016/j.apsusc.2016.01.267]

10. K. Tsuji, M. Nakaya, A. Uedono, and A. Hotta, "Enhancement of the gas barrier property of polypropylene by introducing plasma-treated silane coating with SiO_x-modified top-surface", Surf. & Coatings Tech. 284 (2015) 377-383. [10.1016/j.surfcoat.2015.10.027]

11. M. Nakaya, A. Uedono, and A. Hotta, "Recent progress in gas barrier thin film coatings on PET bottles in food and beverage applications", Coatings 5 (2015) 987-1001. [10.3390/coatings 5040987]

12. A. Uedono, S. Takashima, M. Edo, K. Ueno, H. Matsuyama, H. Kudo, H. Naramoto, and S. Ishibashi, "Vacancy-type defects and their annealing behaviors in Mg-implanted GaN studied by a monoenergetic positron beam", Phys. Status Solidi B 252 (2015) 2794-2801. [DOI: 10.1002/pssb.201552345]

13. T. Selvalakshmi, S. Sellaiyan, A. Uedono, A. C. Bose, “Investigation on photoluminescence, electrical and positron lifetime of Eu^{3+} activated Gd_2O_3 phosphors”, Mat. Chem. Phys. 166 (2015) 73-81. [doi:10.1016/j.matchemphys.2015.09.029]

14. N. Qi, Z. Q. Chen, and A. Uedono, “Molecular motion and relaxation below glass transition temperature in poly (methyl methacrylate) studied by positron annihilation”, Rad. Phys. Chem. 108 (2015) 81-86.

15. A. Sagara, A. Uedono, and S. Shibata, “Thermal behavior of residual defects in low-dose arsenic- and boron-implanted silicon after high-temperature rapid thermal annealing”, IEEE Trans. Semi. Manufacturing 28 (2015) 92-94.

16. C. Ohrt, K. Rätzke, N. Oshima, Y. Kobayashi, B. E. O’Rourke, R. Suzuki, A. Uedono, and F. Faupel, “Free volume profiles at polymer−solid interfaces probed by focused slow positron beam”, Macromolecules 48 (2015) 1493-1498. [DOI: 10.1021/acs.macromol.5b00180]

17. K. Kataoka, M. Kanechika, T. Narita, Y. Kimoto, and A. Uedono, “Positron annihilation and cathodoluminescence study on inductively coupled plasma etched GaN”, Phys. Status Solidi B 252 (2015) 913-916. [DOI: 10.1002/pssb.201451498]

18. K. Kojima, Y. Tsukada, E. Furukawa, M. Saito, Y. Mikawa, S. Kubo, H. Ikeda, K. Fujito, A. Uedono, and S. F. Chichibu, “Low-resistivity m-plane freestanding GaN substrate with very low point-defect concentrations grown by hydride vapor phase epitaxy on a GaN seed crystal synthesized by the ammonothermal method”, APEX 8 (2015) 095501(1-5).

19. A. Uedono, K. Kurihara, N. Yoshihara, S. Nagao, and S. Ishibashi, “Vacancies in $In_xGa_{1-x}N$/GaN multiple quantum wells fabricated on *m*-plane GaN probed by a monoenergetic positron beam”, APEX 8 (2015) 051002(1-4). [doi:10.7567/APEX.8.051002]

20. H. Latiff, A. Horiuchi, M. Kishimoto, H. Yanagihara, E. Kita, “Effect of reaction temperature on particle size of iron oxide nanoparticles via heating of platelet α-FeOOH in tetraethylene glycol” IEEE TransMAG 51 (2015) 5400304.

21. S. F. Chichibu, K. Kojima, Y. Yamazaki, K. Furusawa, and A. Uedono, “Controlling the carrier lifetime of nearly threading-dislocation-free ZnO homoepitaxial films by 3*d* transition-metal doping”, Appl. Phys. Lett. 108 (2016) 021904.

5.2 Proceedings

1. S. Ishibashi and A. Uedono, “Computational studies of positron states and annihilation parameters in semiconductors – vacancy-type defects in group-III nitrides –”, J. Phys.: Conf. Ser. 674(2016) 012020 (1-10). [doi:10.1088/1742-6596/674/1/012020]

2. F. Suzaki, Y. Abe, Z. Ge, D. Nagae, S. Naimi, T. Uesaka, T. Watanabe, M. Wakasugi, K. Yamada, Y. Yamaguchi, J. Zenihiro, Y. Yano, I. Kato, H. Miura, T. Nishimura, S. Omika, T. Suzuki, N. Tadano, Y. Takeuchi, T. Yamaguchi, K. Hiraishi, Y. Ichikawa, T. Moriguchi, A. Ozawa, S. Suzuki, Y. Tajiri, “PERFORMANCE OF A RESONANT SCHOTTKY PICK-UP IN THE COMMISSIONING OF RARE-RI RING”, Proceedings of HIAT2015 (2015) 98-100.

3. H. Miura, Y. Abe, Z. Ge, K. Hiraishi, Y. Ichikawa, I. Kato, T. Moriguchi, D. Nagae, S. Naimi, T. Nishimura, S. Omika, A. Ozawa, F. Suzaki, S. Suzuki, T.Suzuki, N.Tadano, Y. Tajiri, Y. Takeuchi, T. Uesaka, M. Wakasugi, T. Yamaguchi, Y. Yamaguchi, PERFORMANCE OF A FAST KICKER MAGNET FOR RARE-RI RING, Proceedings of HIAT2015 (2015) 95-97.

4. K. Sasa, S. Ishii, H. Oshima, H. Kimura, T. Takahashi, Y. Tajima, Y. Yamato, D. Sekiba, T. Moriguchi, E. Kita, “STATUS OF THE TANDEM ACCELERATOR COMPLEX AT THE UNIVERSITY OF TSUKUBA (UTTAC)”, Proceedings of the 12th Annual Meeting of Particle Accelerator Society of Japan (PASJ2015) (2015) 322-324.

5. K. Sasa, S. Ishii, K. Kita, T. Moriguchi, H. Oshima, D. Sekiba, Y. Tajima, T. Takahashi and Y. Yamato, “Construction of the 6 MV Tandem Accelerator System for Various Ion Beam Applications at the University of Tsukuba”, JACoW, Proceedings of the 13th International Conference on Heavy Ion Accelerator Technology (2015) 285-287.

6. 松中哲也, 笹公和, 末木啓介, 恩田裕一, 石丸隆, 谷口圭輔, 脇山義史, 本多真紀, 高橋努, 松村万寿美, 松崎浩之,「福島原発事故起源ヨウ素 129 の陸域から海洋環境への移行研究」, Proceedings of the 16th Workshop on Environmental Radioactivity, High Energy Accelerator Research Organization (2015) 190-194.

7. 松中哲也, 笹公和, 末木啓介, 高橋努, 松村万寿美, 後藤章夫, 渡邊隆広, 土屋範芳, 平野伸夫, 松崎浩之, 「蔵王山火口湖ヨウ素同位体比の経時変化と火山活動に関する研究」, Proceedings of the 16th Workshop on Environmental Radioactivity, High Energy Accelerator Research Organization (2015) 55-61.

8. 白石智康, 南基泰, 渡邊隆広, 中村俊夫, 朱立平, 松中哲也, 西村弥亜, 「DNAバーコーディングを利用したチベット高原プマユムツォ湖より採取された約15,000年前の湖底柱状堆積物中に含まれた植物片の種同定」, DNA多型 Vol.23 (2015) No.1.

9. 松中哲也，笹公和，末木啓介，高橋努，松村万寿美，後藤章夫，渡邊隆広，土屋範芳，平野伸夫，松崎浩之，「蔵王山における火山活動とヨウ素同位体比の変動」，第17回AMSシンポジウム報告集 (2015) 108-111.

10. 松中哲也，笹公和，末木啓介，高橋努，松村万寿美，大森貴之，松崎浩之，中村俊夫，「GC-AMSの開発と炭素14自動前処理システムの性能評価」，第17回AMSシンポジウム報告集 (2015) 51-55

11. 笹公和，高橋，松中哲也，松村万寿美，泉大希，佐藤志彦，本多真紀，坂口綾，末木啓介，「筑波大学6MV AMSシステムの設置状況と将来展望」，第17回AMSシンポジウム報告集 (2015) 20-23.

12. 泉大希，笹公和，高橋努，松中哲也，佐藤志彦，松村万寿美，末木啓介，戸崎裕貴，三宅泰斗，松崎浩之，「PHITSを用いた^{36}Cl-AMS測定条件の評価と宇宙線生成核種の測定」，第17回AMSシンポジウム報告集(2015) 61-64.

13. 佐藤志彦，末木啓介，笹公和，松中哲也，柴山尚大，泉大希，高橋努，木下哲一，松崎浩之，「^{90}Sr-AMSのための古層抽出を用いた試料精製の検討」，第17回AMSシンポジウム報告集(2015) 69.

14. 松村万寿美，笹公和，松中哲也，高橋努，佐藤志彦,末木啓介，松崎浩之，「AMS試料実験室における^{129}Iの汚染調査」，第17回AMSシンポジウム報告集(2015) 70-73.

15. 本多真紀，末木啓介，松中哲也，坂口綾，笹公和，松崎浩之，「耐圧密閉容器を用いた土壌からの放射性核種抽出法の開発」，第17回AMSシンポジウム報告集(2015) 74-76.

16. 坂口綾，P. Steier，野村知哉，門倉彰伸，渡邊剛，高橋嘉夫，山野博哉，末木啓介，「環日本海における^{236}U」，第17回AMSシンポジウム報告集(2015) 89-93.

17. 渡邊雅也，末木啓介，笹公和，松中哲也，松村万寿美，高橋努，松崎浩之，五十嵐康人，「つくば地域における^{129}I降下量の変動」第17回AMSシンポジウム報告集(2015) 112-115.

18. 富田涼平，末木啓介，笹公和，松中哲也，本多真紀，佐藤志彦，松村万寿美，高橋努，坂口綾，松崎浩之，「原発事故以降の河川における放射性核種と溶存イオンの挙動」第17回AMSシンポジウム報告集(2015) 117-120.

19. M. Matsuo, T. Murayama, K. Koike, S. Sasa, M. Yano, A. Uedono, S. Gonda, R. Ishigami, K. Kume, and T. Ohtomio, 2015 IEEE Int. Meeting for Future of Elec. Dev. KANSAI (IMFEDK), (2015). [ISBN:978-1-4799-8615-6]

5.3 Reviews

1. 山口由高, 若杉昌徳, 阿部康志, 洲嵜ふみ, 長江大輔, 大甕舜一朗, 三浦宙, Naimi SARAH, Ge ZHUANG, 山口貴之, 小沢顕, 上坂友洋, 大西純一, 菊池崇志, 込山美咲, 熊谷桂子, 徳地明, 藤縄雅, 眞家武士, 山澤秀行, 柳澤善行, 渡邉裕, 矢野安重,「理研 RI ビームファクトリー稀少 RI リングの建設」, 日本加速器学会誌「加速器」Vol. 12, No. 3 (2015) 132-141.

2. 大島永康, 鈴木良一, 上殿明良,「陽電子マイクロプローブとその応用」, 放射線と産業 139 (2015) 9-12.

3. 上殿明良,「陽電子消滅による半導体デバイス材料中の空孔型欠陥の評価」, 応用物理 84 (2015) 402-408.

5.4 Books

1. RI ビーム「放射化学の事典」118~120 ページ（担当 小沢顕）, 日本放射化学会編集, 朝倉書店 2015 年 9 月 25 日初版

2. T. Matsunaka, K. Sasa, K. Sueki, Y. Onda. K. Taniguchi, Y. Wakiyama, T. Takahashi, M. Matsumura, H. Matsuzaki, Migration behavior of particulate ^{129}I in the Niida River system, Chapter 6, Radiological Issues for Fukushima's Revitalized Future, Springer (2016) 57-63.

3. S. F. Chichibu, H. Miyake, K. Hiramatsu, and A. Uedono, "Impacts of Dislocations and Point Defects on the Internal Quantum Efficiency of the Near-Band-Edge Emission in AlGaN-Based DUV Light-Emitting Materials", III-Nitride Ultraviolet Emitters: Technology and Applications, Springer Series in Materials Science 227 (2016) 115-136. [10.1007/978-3-319-24100-5_5]

4. 上殿明良, シリコン結晶技術　第 5.3.6 章 陽電子消滅, 日本学術振興会 技術の伝承プロジェクト編集委員会編 福島企画 (2015) 402-405.

5.5 International conferences

1. K. Sueki, N. Shibayama, R. Tomita, Y. Satou, K. Sasa, T. Takahashi, T. Matsunaka, M. Matsumura, H. Matsuzaki, M. Murakami, R. Yamashita, H. Takada, Y. Koibuchi, O. Haecong, G. Mouri, , T. Oki, "Time variation of iodine-129 and radioactive cesium in river water at Ohori River", The International Chemical Congress of Pacific Basin Societies, 15-20 December 2015, Honolulu, USA.

2. Y.Satou, K. Adachi, T. Ono, Y. Iizawa, Y. Abe, I. Nakai, Y. Igarashi, K. Sasa, K .Sueki, “Physicochemical characterizations of radioactive particles emitted at the Fukushima Dai-ichi Nuclear Power Plant accident” The International Chemical Congress of Pacific Basin Societies, 15-20 December 2015, Honolulu, USA.

3. R. Tomita , T. Matsunaka, M. Honda, Y. Satou, M. Matsumura, T. Takahasi, A. Sakaguchi, K. Sasa, K. Sueki and H. Matsuzaki, “Environmental dynamics of dissolved radionuclides and ions in riverine water after the FDNPP accident” The International Chemical Congress of Pacific Basin Societies, 15-20 December 2015, Honolulu, USA.

4. A. Ozawa, “Mass measurements with Rare-RI Ring at RIBF”, 2015 SKLTP-BLTP Joint Workshop on Physics of Strong Interaction, 30 October-2 November 2015, Ronghu Lake Hotel, Guilin, China (invited).

5. K. Sasa, T. Takahashi, M. Matsumura, T. Matsunaka, Y. Satou, M. Honda, D. Izumi, R.Tomita, S. Hosoya, A. Sakaguchi and K. Sueki, “Construction of the 6 MV tandem accelerator for multi-nuclide AMS at the University of Tsukuba”, The 6th East Asia Accelerator Mass Spectrometry Symposium (EA-AMS 6), National Taiwan University, 05-08 October 2015, Taipei, Taiwan (invited) .

6. Y. Satou, K. Sueki, K. Sasa, T. Matsunaka, Takahashi, T., Kinoshita, N. and Matsuzaki, H, “Sample preparation for ^{90}Sr-AMS using solid phase extraction”, 6th East Asia AMS Symposium, 05-08 October 2015, Taipei, Taiwan.

7. M. Honda, K. Sueki, K. Sasa, A. Sakaguchi and H. Matsuzaki, “Developments of analytical methods for ^{36}Cl, ^{129}I, ^{99}Tc in soil samples”, 6th East Asia AMS Symposium, 05-08 October 2015, Taipei, Taiwan.

8. T. Matsunaka, K. Sasa, K. Sueki, T. Takahashi, M. Matsumura, A. Goto, T. Watanabe, N. Tsuchiya, N. Hirano and H. Matsuzaki, “Iodine isotopic ratio in crater lake and geothermal area at Zao volcano, Japan” 6th East Asia AMS Symposium, 05-08 October 2015, Taipei, Taiwan.

9. T. Matsunaka, K. Sasa, K. Sueki, Y. Onda, K. Taniguchi , Y. Wakiyama, T. Takahasi, M. Matsumura, and H. Matsuzaki, “Migration behavior and flux of particulate ^{129}I in the river system of Fukushima.”, 6th East Asia AMS Symposium, 05-08 October 2015, Taipei, Taiwan.

10. M. Matsumura, M. Watanabe, K. Sasa, T. Matsunaka, T. Takahashi, K. Sueki and H. Matsuzaki, “Environmental impact of the Fukushima accident on iodine-129 levels in meteoric water”, 6th East Asia AMS Symposium, 05-08 October 2015, Taipei, Taiwan.

11. T. Matsunaka, K. Sasa, K. Sueki, Y. Onda, T. Ishimaru, K. Taniguchi, Y. Wakiyama, M. Honda, T. Takahasi, M. Matsumura and H. Matsuzaki, “Study on the migration behaviour of Fukushima accident-derived iodine-129 from land area to the marine environment”, International Conference Environmental Radioactivity, 21-25 September 2015, Thessaloniki, Greece.

12. T. Matsunaka, K.Sasa, K. Sueki, T. Takahashi, M. Matsumura, A. Goto, T. Watanabe, N. Tsuchiya, N. Hirano and H. Matsuzaki, “Changes in $^{129}I/^{127}I$ ratio of crater lake and volcanic activity at Zao volcano”, Japan. International Conference Environmental Radioactivity, Thessaloniki, 21-25 September 2015, Thessaloniki, Greece.

13. K. Sasa, M. Matsumura, T. Matsunaka, T. Takahashi, Y. Satou, N. Kinoshita, H. Matsuzaki and K. Sueki, “Estimation of I-131 deposition from I-129 analysis in surface soils released from the Fukushima Daiichi Nuclear Power Plant accident”, International Conference Environmental Radioactivity, 21-25 September 2015, Thessaloniki, Greece.

14. A. Yamazaki, K. Sasa, S. Ishii, M. Kurosawa, S. Tomita, E. Kita, “Development of the Ion Microbeam System for Analysis of Light Elements in Structural Materials at the University of Tsukuba”, SIP-IMASM 2015 symposium, AIST Tsukuba Central 1, The National Institute of Advanced Industrial Science and Technology (AIST), 29 September-1 October 2015, Tsukuba, Japan.

15. A. Ozawa, “Day-one experiment with R3”, OEDO-SHARAQ International Collaboration Workshop, 8-9 September 2015, Tokyo, Japan.

16. K. Sasa, S. Ishii, Hiroyuki Oshima, Yoshikazu Tajima, Tsutomu Takahashi, Yoshihiro Yamato, Daiichiro Sekiba, Tetsuaki Moriguchi and Eiji Kita, “Construction of the 6 MV Tandem Accelerator System for Various Ion Beam Applications at the University of Tsukuba”, 13th Heavy Ion Accelerator Technology Conference (HIAT2015), 7-11 September 2015, Yokohama, Japan.

17. A. Yamazaki, K. Sasa, D. Sekiba, T. Moriguchi, S. Ishii, M. Kurosawa, S. Tomita, E. Kita, “Design of the High Resolution Ion Microbeam System for Analysis of Structural Materials on the 6 MV Tandem Accelerator at the University of Tsukuba”, NIMS Conference 2015, 14-16 July 2015, Tsukuba International Congress Center, EPOCHAL TSUKUBA, Tsukuba, Japan.

18. S. Tomita, R. Kinoshita, Y. Shiina, M. Imai, K. Kawatsura, M. Matsuda, K. Sasa, M. Sataka, “Vicinage Effect on the Generation Mechanism of Convoy Electrons”, SHIM2015, Swift Heavy Ions in Matter , 18-21 May 2015, Darmstadt, Germany.

19. S. Tomita, Y. Nakai, S. Funada, J. O. P. Pedersen, P. Hvelplund, H. Kobara, K. Sasa, “Formation of Nanodroplets in $N_2/H_2O/SO_2$ under Irradiation of Fast Proton Beams”, SHIM2015, Swift Heavy Ions in Matter , 18-21 May 2015, Darmstadt, Germany.

20. T. Matsunaka, K. Sasa, K. Sueki, Y. Onda, K. Taniguchi, Y. Wakiyama, T. Takahasi, M. Matsumura, and H. Matsuzaki, “Migration behavior of particulate ^{129}I in the Niida River system. International Symposium on Radiological Issues for Fukushima's Revitalized Future”, 30-31 May 2015, Fukushima, Japan.

21. T. Matsunaka, K. Sasa, K. Sueki, T. Takahasi, M. Matsumura, Y. Satou, J. Kitagawa, N. Kinoshita, and H. Matsuzaki, “Pre- and post-accident levels of ^{129}I and ^{137}Cs in soil profile near field of the Fukushima Dai-ichi Nuclear Power Plant. International Symposium on Radiological Issues for Fukushima's Revitalized Future”, Japan, 30-31 May 2015, Fukushima, Japan.

22. Y. Satou, K. Sueki, K. Sasa, K. Adachi, Y. Igarashi, “Characterization study of cesium concentrated particles in the soils near the Fukushima Daiichi nuclear power plant”, EGU General Assembly, 12-17 April 2015, Vienna, Austria.

23. Y. Liu, E. Kita, H. Yanagihara, D. Oshima, T. Kato, S. Iwata and K. Mibu, “Magnetization control of $CoFe_2O_4$ thin films by Kr ion implantation”, Joint MMM-Intermag Conference, 11-15 January, 2016, San Diego, California, USA.

5.6 Presentation at academic meetings

1. 笹 公和，高橋 努，松中 哲也，松村 万寿美，坂口 綾，佐藤 志彦，本多 真紀，富田 涼平，細谷 青児，末木 啓介，「6 MV タンデム加速器質量分析システムにおける極微量核種の検出試験」，日本原子力学会 2016 年春の年会，3.26-28, 2016，仙台，東北大学.

2. 鈴木伸司 他,「質量測定用飛行時間検出器の開発」, 日本物理学会第 71 回年次大会, 3.19-22, 2016, 東北学院大学.

3. 石橋陽子 他,「中性子過剰核 ^{39}S の磁気モーメント測定」, 日本物理学会第 71 回年次大会, 3.19-22, 2016, 東北学院大学.

4. 劉 洋，久松 裕季，柳原 英人，大島 大輝，加藤 剛志，岩田 聡，壬生 攻，喜多 英治，“Magnetization control of Co ferrite thin films by Kr ion implantation” 応用物理学会，3.19, 2016, 東京工業大学.

5. 韮澤貴夫, 村上道夫, 吉兼隆生, 末木啓介, 笹公和, 芳村圭，「放射性物質沈着量からの飲食

物由来の被ばく量の推定」，第 50 回日本水環境学会年会（2015 年度），3.16-18, 2016, アスティとくしま，徳島県徳島市.

6. 松中 哲也，笹 公和，末木 啓介，恩田 裕一，高橋 努，松村 万寿美，石丸 隆，谷口 圭輔，脇山 義史，松崎 浩之，「放射性ヨウ素の河川における挙動と沿岸環境中の分布」，日本海洋学会 2016 年度春季大会，3.14-18, 2016，東京大学本郷キャンパス.

7. 松中哲也，「福島の河川と沿岸海洋環境における $^{129}I/^{137}Cs$ 比から推察される放射性のヨウ素とセシウムの挙動」，平成 27 年度第 2 回 Iset-R 全体会議，3.11-12, 2016, つくば市.

8. Matsumura, M., “Environmental impact of the Fukushima accident on iodine-129 levels in meteoric water”，平成 27 年度第 2 回 Iset-R 全体会議，3.11-12, 2016, つくば市.

9. 松中 哲也，笹 公和，末木 啓介，高橋 努，佐藤 志彦，松村 万寿美，松崎 浩之，「福島県浪江町における年輪中の炭素 14 濃度変動」, 第 17 回「環境放射能」研究会，3.8-10, 2016, KEK，つくば市.

10. 村上道夫, 韮澤貴夫, 吉兼隆生, 末木啓介, 笹公和, 芳村圭，「仮想的な原子力発電所事故における飲食物由来の被ばく量の推定」，第 2 回福島大学環境放射能研究所成果報告会，3.7, 2016，コラッセふくしま.

11. 細谷 青児，笹 公和，松中 哲也，松村 万寿美，高橋 努，Mark Sundquist, Mark Stodola, 末木 啓介，「難測定核種 AMS 開発に向けた PHITS シミュレーションの適用」，第 18 回 AMS シンポジウム，3.4-5, 2016，東京大学.

12. 笹 公和，高橋 努，松中 哲也，松村 万寿美，坂口 綾，佐藤 志彦，本多 真紀，富田 涼平，細谷 青児，末木 啓介，「筑波大学 6 MV 加速器質量分析システムの現状と AMS 試験測定結果」，第 18 回 AMS シンポジウム，東京，3.4-5, 2016，東京大学.

13. 松中 哲也，笹 公和，高橋 努，松村 万寿美，末木 啓介，松崎 浩之，「福島における西暦 2010 年の晩材に記録された $\Delta^{14}C$ 増大」，第 18 回 AMS シンポジウム，3.4-5, 2016，東京大学.

14. 松中 哲也，笹 公和，高橋 努，松村 万寿美，末木 啓介，後藤 章夫，渡邊 隆広，土屋 範芳，平野 伸夫，久利 美和，高橋 正明，風早 康平，宮城 磯治，松崎 浩之，「蔵王山における火口湖と地熱帯で観測されたヨウ素同位体比の低下」, 第 18 回 AMS シンポジウム，3.4-5, 2016，東京大学.

15. 松村 万寿美，渡邊 雅也，笹 公和，松中 哲也，高橋 努，末木 啓介，松崎 浩之，[福島第一原子力発電所事故によるヨウ素 129 の降水への影響], 第 18 回 AMS シンポジウム，3.4-5,

2016, 東京大学.

16. Matsunaka, T., “Migration behavior of radioiodine and radiocesium in river system and coastal marine environments of Fukushima”, 第 8 回アイソトープ環境動態研究センター研究部門セミナー, 2016.1.12, つくば市.

17. 土田秀次, 間嶋拓也, 冨田成夫, 笹公和, 平田浩一, 柴田裕実, 鳴海一雅, 斉藤勇一, 千葉敦也, 山田圭介, 的場史朗, 伊藤秋男, [キャピラリー帯電効果による C60 ビームの静電偏向], 日本物理学会秋の大会, 9.16-19, 2015, 関西大学.

18. Shigeo Tomita, Yoko Shiina, Ryo Kinoshita, Makoto Imai, Kiyoshi Kawatsura, Makoto Matsuda, Kimikazu Sasa, and Masao Sataka, “Zero degree electron spectroscopy of fast carbon clusters through carbon foil”, 第 16 回「イオンビームによる表面・界面」特別研究会, 12.5-6, 2015, 奈良女子大学.

19. 松中 哲也, 笹 公和, 末木 啓介, 高橋 努, 佐藤 志彦, 松村 万寿美, 松崎 浩之, 「過去 7 年間にわたる福島県浪江町の年輪中の炭素 14 濃度変動」, 日本放射線安全管理学会 第 14 回学術大会, 12.2-4, 2015, 筑波大学, つくば市.

20. 松村 万寿美, 笹 公和, 末木 啓介, 松中 哲也, 高橋 努, 佐藤 志彦, 松崎 浩之, 「ヨウ素 129 による経時的汚染調査 - 加速器質量分析用の試料処理実験室の場合 - 」, 日本放射線安全管理学会 第 14 回学術大会, 12.2-4, 2015, 筑波大学, つくば市.

21. 笹 公和, 大島 弘行, 森口哲郎, 高橋 努, 松村 万寿美, 松中 哲也, 末木 啓介, 喜多 英治, 「筑波大学 6 MV タンデム加速器の建設と極微量核種検出システムの開発」, 日本放射線安全管理学会 第 14 回学術大会, 12.2-4, 2015, 筑波大学, つくば市.

22. 佐藤 志彦, 末木 啓介, 笹 公和, 箕輪 はるか, 吉川 英樹, 藤原 健壮, 中間 茂雄, 足立 光司, 五十嵐 康人, 「福島第一原発周辺で見つかった放射性粒子の特徴」, 日本放射線安全管理学会 第 14 回学術大会, 12.2-4, 2015, 筑波大学, つくば市.

23. 森口哲朗, 笹公和, 大島弘行, 喜多英治, 「筑波大学 12UD ペレトロンタンデム加速器の廃止措置計画」, 日本放射線安全管理学会 第 14 回学術大会, 12.2-4, 2015, 筑波大学, つくば市.

24. M. Honda, K. Sueki, K. Sasa, A. Sakaguchi, H. Matsuzaki, A new extraction method for ^{36}Cl, ^{129}I and ^{99}Tc in soil samples with microwave assisted digestion equipment, 日本質量分析学会同位体比部会 2015, 11.25-27, 2015, 大津市.

25. 松中哲也，「放射性ヨウ素129の陸から海洋への移行研究」，平成27年度第1回ISET-R海洋合同班会議, 10.23-24, 2015, 神戸市.

26. 富田 涼平, 松中 哲也, 本多 真紀, 佐藤 志彦, 松村 万寿美, 高橋 努, 坂口 綾, 松崎 浩之, 笹 公和, 末木 啓介, 「発事故以降の都市部河川における放射性核種と溶存イオンの挙動」, 2015 日本放射化学会年会・第 59 回放射化学討論会, 9.25-27, 2015, 東北大学, 仙台市.

27. 本多 真紀, 末木 啓介, 坂口 綾, 笹 公和, 松崎 浩之, 「難測定核種である塩素 36, ヨウ素 129, テクネチウム 99 の土壌からの抽出方法の検討」, 2015 日本放射化学会年会・第 59 回放射化学討論会, 9.25-27, 2015, 東北大学, 仙台市.

28. 佐藤 志彦, 足立 光司, 小野 貴大, 飯澤 勇信, 阿部 善也, 中井 泉, 五十嵐 康人, 笹 公和, 末木 啓介, 「福島第一原発事故で放出した放射性粒子の発生源による違い」, 2015 日本放射化学会年会・第 59 回放射化学討論会, 9.25-27, 2015, 東北大学, 仙台市.

29. 松中 哲也, 笹 公和, 末木 啓介, 恩田 裕一, 石丸 隆, 谷口 圭輔, 脇山 義史, 高橋 努, 松村 万寿美, 松崎 浩之, 「福島原発起源ヨウ素 129 の陸域から海洋への移行研究」, 2015 年度日本地球化学会年会, 9.16-28, 2015, 横浜市.

30. 佐藤 志彦, 末木 啓介, 笹 公和, 小野 貴大, 飯澤 勇信, 阿部 善也, 中井 泉, 足立 光司, 五十嵐 康人, 「福島第一原発事故で放出した放射性粒子の特徴」, 2015 年度日本地球化学会年会, 9.16-28, 2015, 横浜市.

31. 鈴木伸司 他, 「RI ビーム飛行時間検出器の開発」, 日本物理学会 2015 年秋季大会, 9.25-28, 2015, 大阪市立大学.

32. 黒澤正紀, 「顕微ラマン分光法による多相包有物中の固相の分析」, 日本鉱物科学会, 9.26, 2015, 東京大学.

33. 三宅 亮 他, 「対馬花崗岩体における晶洞石英中の多相流体包有物の観察および分析」, 日本鉱物科学会, 9.27, 2015, 東京大学.

34. 小沢顕, Present status of Rare-RI Ring project at RIBF, 「実験と観測で解き明かす中性子星の核物質」第 4 回研究会, 9.17-18, 2015, 湘南国際村センター.

35. 森口哲朗, 「筑波大学イオン加速器システムによる計測手法」, 第 1 回光・量子計測シンポジウム, 9.9, 2015, つくば国際会議場, つくば市.

36. 松中哲也, 「福島原発起源ヨウ素 129 の陸域から海洋への移行研究」, ISET-R 第 9 回 A04-08

班・班会議，2015.8.10, 2015, 大阪.

37. 笹 公和，石井 聰，大島 弘行，木村 博美，高橋 努，田島 義一，大和 良広，関場 大一郎，森口 哲朗，喜多 英治，「筑波大学マルチタンデム加速器施設の現状」，第 12 回日本加速器学会年会，8.5-7, 2015, 敦賀市.

38. 笹 公和，石井 聰，大島 弘行，木村 博美，高橋 努，田島 義一，大和 良広，関場 大一郎，喜多 英治，「筑波大学タンデム加速器施設 UTTAC の現状(2014 年度)」，第 28 回タンデム加速器及びその周辺技術の研究会，7.3-4, 2015, 東北大学，仙台市.

39. 森口哲朗，笹 公和，大島弘行，石井 聰，高橋努，田島義一，大和良広，関場大一郎，喜多英治，「筑波大学 UTTAC におけるタンデム加速器の廃止措置計画」，第 28 回タンデム加速器及びその周辺技術の研究会，7.3-4, 2015, 東北大学，仙台市.

40. 山崎明義，笹 公和，石井 聰，黒澤正紀，冨田成夫，喜多英治，工藤 博，楢本 洋，左高正雄，「筑波大学 6MV タンデム加速器マイクロビームラインの建設計画」，第 28 回タンデム加速器及びその周辺技術の研究会，7.3-4, 2015，仙台市.

41. 佐藤 志彦，末木 啓介，笹 公和，足立 光司，五十嵐 康人，「福島第一原発周辺で採取した土壌から分離した放射性微粒子の同定」，日本地球惑星科学連合 2015 年大会，5.26, 2015, 幕張メッセ国際会議場，千葉市.

42. 笹 公和，「福島第一原発事故により放出された ^{129}I の陸域環境での分布」，Iset-R 全体会議，5.25, 2015，幕張，千葉市.

43. 松中哲也，笹公和，「ガスクロマトグラフ–加速器質量分析法の開発と炭素 14 自動前処理システムの性能評価」，第三回放射性炭素年代測定室ワークショップ，5.20-23, 2015, つくば市.

44. 笹 公和，「筑波大学における 6MV タンデム加速器を用いた加速器質量分析法」，第四紀学会講習会 第三回放射性炭素年代測定室ワークショップ，5.20-23, 2015，つくば市.

45. 藤本恭輔 他，「対馬花崗岩体における晶洞石英中の多相流体包有物分析」, 日本地球惑星科学連合大会，5.24-28, 2015，幕張メッセ，千葉市.

46. 小沢顕，「RI ビーム飛行時間検出器の開発」，H26 年度 HIMAC 共同利用研究成果発表会，4.20-21, 2015, ホテルポートプラザちば，千葉市.

47. 小沢顕，「固体水素標的を用いた陽子ドリップライン近傍核生成法の開発」，H26 年度 HIMAC 共同利用研究成果発表会，2015, 4.20-21，ホテルポートプラザちば，千葉市.

6.

THESES

Doctor theses

Yasushi Abe	Study of isochronous field in Rare-RI Ring for high-precision mass measurements.
Yukihiko Satou	Study of relationship between deposition of radioactive materials and radioactive particles in the difficult-to-return zone caused by the Fukushima Dai-ichi Nuclear Power Plant accident.

Master theses

Yukina Ichikawa	Developments of time-of-flight detector using crossed electric and magnetic fields.
Hawa Alima Latiff	Synthesis and physical properties of functional spinel ferrite particles
Katsuya Yamazaki	Detection of biomolecular ions using superconducting tunnel junction detectors
Satomi Maeda	Hydrogen observation by HERDA to elucidate hydrogen desorption mechanism on Pd(110)

Undergraduate theses

Yoshiyuki Tajiri	Developments of time-of-flight detector using mass measurements in Rare-RI Ring.
Kentaro Hiraishi	Production of unstable nuclei ^{30}P by using resonant proton capture reaction.
Takuya Matsumoto	Production of unstable nuclei ^{25}Al by using resonant proton capture reaction.
Seiji Hosoya	Development of AMS measuring condition using the PHITS code and measurement of cosmogenic nuclides.
Yuhi Asakawa	Zero degree electron spectroscopy of fast cluster ions
Naoki Yamamoto	Experiments of electron–molecule collisions using electrostatic ion storage ring
Koki Tsujita	Development of preamplifier for multichannel solid state detector in high-sensitivity HERDA
Keisuke Nishio	Chemical features of early solar nebular gas components recorded in glass inclusions from carbonaceous chondrites.
Koichi Hattori	Geochemical exploration method for sea-floor hydrothermal ore deposits.

7.

LIST OF PERSONNEL

Tandem Accelerator Complex

E. Kita	Director, Professor
K. Sasa	Associate Professor
D. Sekiba	Lecturer
T. Moriguchi	Assistant Professor
H. Oshima	Electrical Engineer
Y. Tajima	Mechanical Engineer
S. Ishii	Mechanical Engineer
T. Takahashi	Electrical Engineer
Y. Yamato	Electrical Engineer
M. Sataka	Research Fellow
M. Matsumura	Research Supporter
M. Ohyama	Administrative Staff
N. Yamada	Administrative Staff
H. Muromachi	Administrative Staff

Research Members[1]

Inst. of Physics

I. Arai	A. Ozawa	T. Matsunaka	T. Moriguchi
K. Sasa	S. Suzuki	P. Schury	

Inst. of Applied Physics

S. Sellaiyan	E. Kita	A. Kashihuku	D. Sekiba
S. Sharmin	S. Tomita	A. Uedono	H. Yanagihara

Inst. of Geoscience

M. Kurosawa

Inst. of Chemistry

K. Sueki A. Sakaguchi

Staff of Open Advanced Facilities Initiative

H. Kudo H. Naramoto M. Sataka

K. Awazu (National Institute of Advanced Industrial Science and Technology [AIST])

S. Aoki (Comprehensive Research Organization for Science and Society [CROSS])

[1] The “research members” include the authors and coauthors within 5 years back from this fiscal year, as well as the members of research projects running at UTTAC.

Staff of Joint Research Projects with Other Organizations

A. Yamazaki (Cross-ministerial Strategic Innovation Promotion Program [SIP])[2]

Y. Watahiki (Nanotech Career-up Alliance [CuPAL])

Graduate students

Doctoral Programs of Pure and Applied Science

M. Ahmed	F. Arai	S. Fukuoka	I. Harayama
Y. Ishibashi	Y. Shiina	S. Kimura	M. Mukai
M. Honda	Y. Satou	Y. Liu	R. Patel

Master's Programs of Pure and Applied Science

H. Latiff	R. Aoyama	Y. Asakawa	Y. Ichikawa
T. Kakizaki	T. Kuroiwa	S. Maeda	M. Matsumoto
T. Murayama	E. Noguchi	S. Nomoto	M. Oka
K. Okada	T. Sennba	S. Sakai	T. Tamura
R. Tomita	T. Tanoishou	K. Yamazaki	

Undergraduates

T. Eguchi	K. Hiraishi	Y. Hosoi	S. Hosoya
N. Hiruta	H. Onoda	Y. Tajiri	K. Tsujita
N. Yamamoto			

Scientific Guests and Fellows

Y. Tosaki	National Institute of Advanced Industrial Science and Technology (AIST)
H. Matsumura	High Energy Accelerator Research Organization (KEK)
N. Kinoshita	SHIMIZU Corporation
K. Hirata	National Institute of Advanced Industrial Science and Technology (AIST)
T. Omori	The University of Tokyo
R. Katayama	The University of Tokyo
K. Ozeki	Ibaraki University

[2] Also, a staff of *Open Advanced Facilities Initiative*